이학박사 학위논문

Fluid Dynamic Properties of Nanoconfined Water

나노컨파인드 물의 유체 동역학적 성질

2014년 2월

서울대학교 대학원

물리·천문학부

김 봉 수

Fluid Dynamic Properties of Nanoconfined Water

나노컨파인드 물의 유체 동역학적 성질

指導敎授 諸元鎬

이 論文을 理學博士學位論文으로 提出함

2013年 11月

서울大學校 大學院

物理·天文學部

金 奉 洙

金奉洙의 理學博士 學位論文을 認准함

2013年 12月

委 員 長	홍 승 훈	印
副委員長	제 원 호	印
委 員	박 건 식	印
委 員	유 재 준	印
委 員	곽 호 영	印

Fluid Dynamic Properties of Nanoconfined Water

by

Bongsu Kim,

Dissertation

Presented to the Faculty of the Graduate School of

Seoul National University

in Partial Fulfillment

of the Requirements

for the Degree of

Doctor of Philosophy

Seoul National University

February 2014

Abstract

Fluid Dynamic Properties of Nanoconfined Water

Bongsu Kim
Department of Physics and Astronomy
The Graduate School
Seoul National University

Most of the nano-metric confined space is filled with liquid water called nanoconfined water in ambient condition, to say nothing of liquid water enviroment. The ubiquitous nanoconfined water naturally plays an important role for various mechanisms such as biological processes, swelling clays, colloidal interaction, and friction. In the 21st Century, the study of the nanoconfined water has begun in earnest due to the development of techniques to control stable nanoconfined space in ambient or liquid condition. Meanwhile reported properties of nanoconfiend water are summarized as follows. (i) enhanced viscosity $10^2 \sim 10^7$ times larger compared with bulk water, (ii) sluggish relaxation time ($10^{-2} \sim 10^{-9}$ s), (iii) nonlinear viscoelasticity, and (iv) violence of classic interfacial force. Although the various properties have been phenomenologically known, however, (1) the fundamental understanding of characteristics or the understanding of the relation between properties are still insufficient. And, (2) until now, the slow velocity (< 1 μm/s) experiments are performed only even though more fast-velocity friction frequently occurs in nature.

In this study, (1) the unified stress tensor of nanoconfined hydration water layer (HWL), which shows the relation between characteristics of HWL and leads the other physical quantities by relation between tapping and shear properties, is introduced and demonstrated using quartz tuning fork based atomic force microscopy (QTF-AFM). And, (2) through fast velocity ($\sim$ 1 mm/s) experiments, the nanoscale elastic turbulence, which is marvelous phenomenon since it is impossible in Newtonian flow, is observed. Moreover the autoregulation in capillary, which is phenomenon that blood flow velocity is maintained automatically despite of a blood pressure change, may be understood through the nanoscale elastic turbulence between red blood cell and capillary wall.

The study about unified stress tensor would contribute not alone nanoconfined water but methodology of various viscoelastic material studies. And elastic turbulence in nanoconfined water would be considered in various fields where nanoconfiend water exists. In particular, the physical understainding of autoregulation in capillary is anticipated to expand understanding of brain science such as cerebral infarction or Alzheimer's disease.

Keywords : Nanoconfined water, Hydrated water layer, Viscoelasticity, Elastic turbulence, Atomic force microscope

Student number : 2007-20410

Contents

List of Figures

Chapter 1

Introduction

Over the last 10 years, various direct force-measuring techniques, such as surface force apparatuses(SFA) or atomic force microscope(AFM), allow us to study a confined water between two surfaces at the nano and angstrom resolution level. Especially, the debate of a magnitude of viscosity of nano-metric confiend water had continued until recently. Historically, the mechanical properties of nano-metric confined water were proposed by J. N. Israelachvili, et al. (1986) using SFA [1]. They measured that the viscosity of the confined thin water film under 10 nm is similar with bulk value. However, the viscosity of confiend water under 5 nm was still unrevealed. In the 21 century, the confined thin water film was explored up to few angstroms using the developed SFA and modified version of one (SFB, surface force balance). First, in August 2001, S. Granick and Y. Zhu measured the viscosity of 1$\sim$2 water molecules layer (Distance between water molecules in liquid water is about 0.27 nm) between mica surfaces by shear

motion using SFA, and they observed that amazing enhanced viscosity was $10^5 \sim 10^9$ times larger than the bulk water value [2]. Interestingly, in Semtember the same year, J. Klein et al. reported the measured that the viscosity of confined water under 1 nm by squeezing effect using SFB is similar with bulk value [3]. It was thought that extreme difference between the measurements of the two group was resulted in the distinction of measuring methods. However J. Klein et al. reported and argued that the viscosity under 1 nm was still remained bulk value in shear motion of SFB (In this paper the measured viscosity was about 80 times larger than bulk value) [4]. This debate was connected to experiments using scanning probe microscopy (SPM) and computer simulation. After 4 years (2006), Y. Zhu and co-workers remeasured viscosity under 1 nm using interfacial force microscopy (IFM) and it turned out 7 orders of magnutude grater than taht of bulk water [5]. This report has a meaning since it is the first result from other experimental equipment rather than SFA or SFB. After that various AFM experiments are executed in water or solutions, and every data shows that the viscosity in confined water under 1$\sim$2 nm between silica tip and mica substrate is larger (over 100 times) than bulk value [6–9]. In addition, molecular dynamic (MD) simulations also show the enhanced viscosity of sub-nano metric confined water between mica surfaces. Y. Leng and P. T. Cummings performed MD simulations to investigate the shear dynamics of nanoconfined water between mica surfaces similar with SFA and SFB. In 2005, they obtained about 80 times larger value of bulk viscosity where water layer thickness is about 0.92 nm [10]. This result coincides with SFB experiments (nanoconfiend water has the similar

visosity of bulk water) [4]. However, next year, they reported greatly enhanced viscosity ($> 1,000$ times) in 0.61 nm of the same system [11]. As a result, various experiments and MD simulation lead to the inescapable conclusion that nanoconfiend water has enhanced viscosity and behaves differently with bulk water.

Over a decade, while the debate about viscosity of nanoconfined water is animated, various other mechanical properties of nanoconfined water(NCW) also had revealed. S. Granick and co-workers reported that NCW has the elastic property and sluggish relaxation time [2]. At first they expected that ice-structure would be observed between mica surfaces since "ice-structure" on (not between) mica surface was predicted previously by MD simulation [12], and observed using infrared spectra [13]. Instead, they reported NCW was highly visous, had the sluggish relaxation time [2]. These properties of NCW is similar with supercooled water [14] rather than stable bulk water. Similarity between NCW and supercooled water was directly mentioned at first by T. D. Li and E.Riedo [7]. Using AFM, they showed that NCW between silica and mica has the sluggish relaxation time and nonlinear viscoelasticity. In Rheology(academic field about mechanical nonlinear viscoelastic flow), the viscosity of supercooled water (or liquid) decreases with increasing shear rate when shear rate exceeds a reciprocal relaxation time, this phenomenon is called "shear thinning". Namely, if relaxation time is long, the shear thinning appers at low shear rate. E. Riedo and co-workers were obtained shear thinning and slow relaxation time ($\sim$10 ms) in NCW [7]. However M. A. Ricci and co-workers pointed out that distinct dif-

ferences between NCW and supercooled water also exsisted [15]. Nevertheless, until recently supercooled liquidity of NCW is a interesting topic [16].

Other important characteristic is a hydration force. The Derjaguin-Landau-Verwey-Overbeek(DLVO) theory successfully explained experimental data of the long range (over 5 nm gap) forces in water and various aqueous systems, such as lipids, clays and colloids, in terms of electrostatic force and van der Waals force [17]. However the short-range interactions under 1∼3 nm gap are still in a debate [17,18]. According to DLVO theory, the more the distances between surfaces are closer, the more the van der Waals force becomes dominant; consequently the surfaces come into a contact. But the strong repulsive forces were measured between surfaces in the short-range distance in many experiments [2, 4, 17, 19] which force is called the hydration force. Empirical form of the hydration force is very simple, but origins of one are still not clarified [17,18].

This thesis is laid on above-mentioned history of the nanoconfined water. Meanwhile, the understanding of nanoconfined water diversifes. However, an understanding of relations between each observation is insufficient since it has been studied either in shear or tapping mode individually. In Chapter 2, Quartz tuning fork (QTF) based atomic force microscopy (AFM) used for experiments is explained. Then, in Chapter 3, the stress-strain tensor (H_{ik}) of nanoconfined hydration water layer is introduced and demonstrated with experiments of shear and tapping mode. H_{ik} affords the understanding of relations of between various experiments, such as tapping and shear motion, and new physical quantities, Poisson's ratio and volume viscosity, are obtained from the relations. In Chapter

4, the turbulence observed in nanoconfined water is studied. The huge velocity is required for a transition to a turbulence in samll systems. It is actually impossible that the nano water film is transformed to the turbulence since 10^6 m/s flow velocity is needed. However, the turbulence in nanoconfined water could be revealed via elasticity, without inertia, and to trigger this transition, about 1mm/s flow velocity is big enough. The nanoscale turbulence is an important factor in understanding of autoregulation in capillary. Red blood cells are on average 25% larger than capillaries [20], in which they become severely deformed and literally plugging [21] so that nanometric plasma (water) layer forms between Red blood cells and less-deformable capillary endothelium that lacks muscle cells [22]. Therefore, fundamental mechanism for autoregulation has been a longstanding enigma beyond possible pathological origins [23, 24], and fluid dynamics of plasma layer still remains unaddressed despite its crucial role in blood rheology [25] and autoregulation. Our results offer first-principle understanding that ultrathin plasma layer induces universal autoregulated velocity ($\sim$1 mm/s).

Bibliography

[1] J. N. Israelachvili, J. Colloid and Interf. Sci. **110**, 263 (1986).

[2] S. Granick, Phys. Rev. Lett. **87**, 096104 (2001).

[3] U.Raviv, P. Laurat, and J. Klein, Nature **51**, 413 (2001).

[4] U.Raviv, and J. Klein, Science **297**, 1540 (2002).

[5] R. C. Major, J. E. Houston, M. J. McGrath, J. I. Siepmann, and X.-Y. Zhu, Phys. Rev. Lett. **96**, 177803 (2006).

[6] H. Sakuma, K. Otsuki, and J. Jurihara, Phys. Rev. Lett. **96**, 1046104 (2006).

[7] T. Li, J. Gao, R.T. Szoszkiewicz, U. Landman, and E. Riedo, Phys. Rev. B **75**, 115415 (2007).

[8] T. Li and E. Riedo, Phys. Rev. Lett. **100**, 106102 (2008).

[9] S. H. Khan, G. Matei, S. Patil, and P. M. Hoffmann, Phys. Rev. Lett. **105**, 106101 (2010).

[10] Y. Leng and P. T. Cummings, Phys. Rev. Lett. **94**, 026101 (2005).

[11] Y. Leng and P. T. Cummings, J. Chem. Phys. **125**, 104701 (2006).

[12] M. Odelius, M. Bernasconi, and M. Parrinello, Phys. Rev. Lett. **78**, 2855 (1977).

[13] W. Cantrell and G. E. Ewing, J. Phys. Chem. B **105**, 5434 (2001).

[14] Debenedetti, Pablo, *Metastable Liquids: Concepts and Principles* (Princeton University Press, 1996)

[15] M. A. Ricci, F. Bruni, and A. Giuliani, Faraday discuss. **141**, 347 (2009).

[16] S. Granick, S. Bae, S. Kumar, and C. Yu, Physics **3**, 73 (2010).

[17] J. N. Israelachvili *Inatermolecular and surface forces 3rd edi.* (Elsevier Press, 2011).

[18] J. Faraudo and F. Bresme, Phys. Rev. Lett. **94**, 077802 (2005).

[19] R.G. Horn, D.T. Smith and W. Haller, Chem. Phys. Lett. **162**, 404 (1989).

[20] G. Snyder and B. Sheafor, Amer. Zool. **39**, 189 (1999).

[21] R. Skalak and P. Branemark, Science **164**, 717 (1969).

[22] R. Whitmore, Nature **215**, 123 (1967).

[23] C. Peppiatt, C. Howarth, P. Mobbs, and D. Attwell, Nature **443**, 700 (2006).

[24] F. Fernandez-Klett, N. Offenhauser, U. Dirnagl, J. Priller, and U. Lindauer, Proc. Atl. Acad. Sci. **51**, 2290 (2010).

[25] G. Mchedlishvili, M. Varazashvili, A. Mamaladze, and N. Momtselidze, Microvas. Res. **53**, 201 (1997).

Chapter 2

QTF-AFM

2.1 Quartz tunning fork (QTF)

Quartz tunning fork (QTF) is an electomechanical resonaor which is widely used a force senor in various fields such as atomic force microscopy [1] and electrostatic force microscopy [2]. Especially, as AFM probe, QTF has demonstrated the subatomic resolution imaging of the charge distribution of a single atom [3], and high stiffness and sensitivity of QTF allow experiments without jump-to-contact in ambient condition [4]. However, although there have been several attemps to use QTF, it is carefully dealt for quantitative force sensor since a motion of QTF is not simply converted to electrical signal [5]. Here, it is introduced how the electic output signal of QTF could be transform to real harmonic motion of QTF.

Figure 2.1 (a) is a picture of QTF which has two separated terminals, and

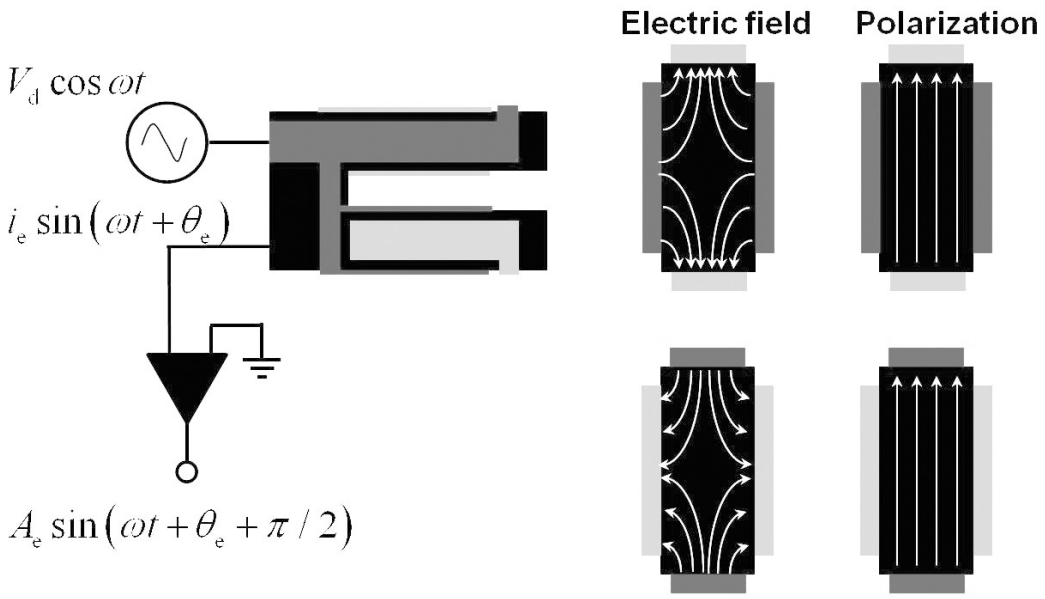

Figure 2.1: The structure of quartz tuning fork (QTF). QTF is made to vibrate by small oscillating voltages applied to metal electrodes plated on the surface of the crystal. The quartz is expanded (contracted) with a polariztion direction when The electric field form same (opposite) direction with polariztion of quartz since quartz is piezoelectric.

each termianl is connected to elctrodes on QTF. When one termianl is ellectrically driven oscillating motion, QTF responds for oscillating motion. However the electrical additive capacitance (C_0) is arisen by connected to elctrodes on QTF (Figure 2.2). This is a just electric problem thus it could be also resolved by parallel connection of a same magnitude capacitance with a phase shifter [6]. Or simply effects of additive capacitance is removed by electrical circuit problem [5]. Figure 2.2 (b) is a model circuit for QTF. The circuit is composed RLC (simple harmonic motion of QTF) and C_0 which is typically used as a model circuit for quartz resonators [7]. Let the total current I_e is $I_e = A_e \sin(\omega t + \theta_e)$

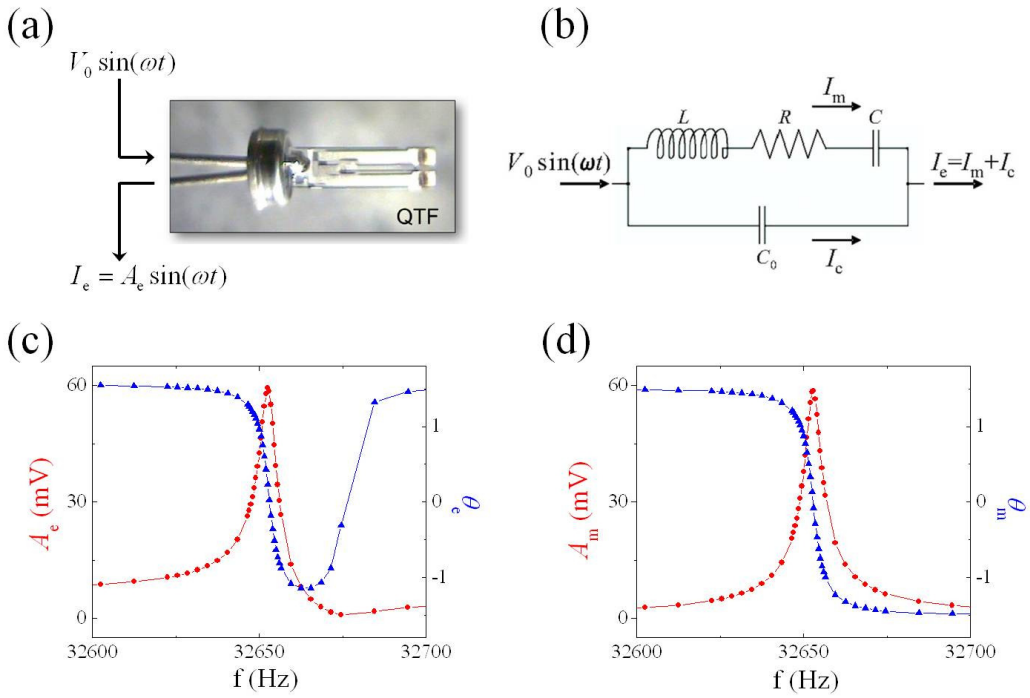

Figure 2.2: Quartz tunning fork (QTF) (a) Picture of QTF resonator which has two prongs. When one terminal is electrically driven oscillating motion, then QTF responds for oscillating motion. Then another terminal give signal of QTF motion. (b) Model cicuit for ellectrically driven QTF. QTF osillates for simple harmonic motion, but output signal include nonlinear term due to additive capacitance (C_0) between electrodes on QTF. (c) Output electrical signal of QTF. The eletrical amplitude and phase of the output signals are include the signal via additive capacitance. (d) Converted mechanical signals of QTF. The signals of QTF mechanmical motion could be obtained by soving the electonic circuit problem.

when driven voltage is $V_0 = \sin(\omega t)$. Since $I_e = I_m + I_c$, I_m is obtained as $A_e \sin(\omega t - \theta_e) + \omega C_0 V_0 \sin(\omega t)$. Then the following quantities are obtained:

$$A_m = \sqrt{A_e^2 - 2\omega C_0 V_0 A_e \sin(\theta_e) + (\omega C_0 V_0)^2}, \tag{2.1}$$

$$\theta_m = \arg[A_e \cos(\theta_e) + i(A_e \sin(\theta_e) - \omega C_0 V_0)]. \tag{2.2}$$

Figure 2.2 (c) is the resonance curve of the output eletric signal($I_e = \sin(\omega t - \theta_e)$) of QTF which include the effect of additive capacitance (C_0), therefore it shows the highly nonlinearity. Figure 2.2 (d) is the transformed resonance curve which is removed the effects of (C_0), thus the resonance curve becomes one of simple harmonic motion. These are the amplitude (A_m) and phase(θ_m) of the real motion of QTF.

2.2 QTF based Amplitude Modulation Atomic Force Microscopy (AM-AFM)

The electrically converted output signal of the QTF from the mechanical properties (viscoelasticity) of target materials exerting on the apex of the tip can be interpreted by amplitude modulation (AM) [8] and frequency modulation (FM) [9] mode of QTF-AFM using a approximating model of a harmonic oscillator. In this work, I used the nanopipette tip attached on a prong of QTF in Fig. 2.3 (a). The QTF operates in two different modes: tapping (Fig. 2.3 (b)) and shear modes(Fig. 2.3 (c)).

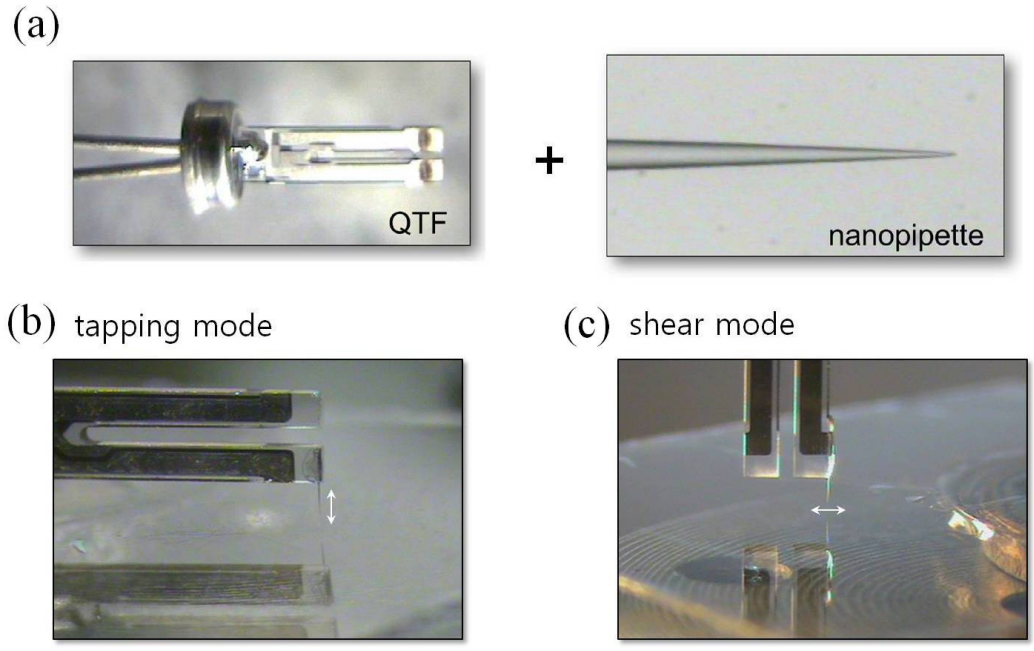

Figure 2.3: QTF-AFM system (a) Piezoelectric device of QTF combines with the pulled nanopipette. (b), (c) The tapping- and shear-mode operation of the QTF-based AFM. The tapping tip oscillates vertically to the mica surface, while the shearing tip vibrates parallel to the surface.

AM-AFM is a dynamic force microscopy where the probe tip is excited by an external driving force with fixed amplitude and frequency. The response amplitude and the phase shift of the QTF are obserbable quantities that reflect interactions between tip and other target materials. Gnerally, effective elasticity and damping coefficient of the target materials are obtained by the response amplitude and the phase shift. And the converting process from the response amplitude and the phase shift to effective elasticity and damping coefficient is the same regardless of mode (tapping and shear). The QTF response can be easily interpreted by analysis of the following equation of motion;

$$m\ddot{x} + b\dot{x} + kx = F\cos\omega t + F_{\rm int}(x, \dot{x}), \tag{2.3}$$

where m is the effective mass of the probe, b, k are the damping coefficient and the spring constant of QTF, F is the amplitude of the drive, and $F_{\rm int}(x, \dot{x})$ is the interaction force. Note that these constants can be expressed in terms of experimental quantities; $m = k/\omega_0^2$, $b = k/(Q\omega_0)$, and $F = kA_0/Q$, where ω_0, Q, and A_0 are the resonance frequency, quality factor, and free oscillation amplitude. Generally any interaction force can be also expanded with the Taylor series:

$$\begin{aligned} F_{\rm int}(x_0 + \Delta x, \dot{x}_0 + \Delta\dot{x}) &\approx F(x_0, \dot{x}_0) + \frac{\partial F}{\partial x}\Delta x + \frac{\partial F}{\partial \dot{x}}\Delta\dot{x} \\ &\equiv F(x_0, \dot{x}_0) - k_{\rm int}\Delta x - b_{\rm int}\Delta\dot{x}. \end{aligned} \tag{2.4}$$

If we focus on the harmonic motion of the probe, we obtain the solution of the

form,

$$x = x_0 + A\sin(\omega t + \theta) \tag{2.5}$$

$$\dot{x} = A\omega\cos(\omega t + \theta)$$

where A is the amplitude of tip, θ phase shift, ω driven angular frequency. Inserting Eq.(2.4) and Eq.(2.5) into into Eq.(2.3) then and multiplying both sides of the resulting equation by $\sin[\omega t + \theta]$ and $\cos[\omega t + \theta]$, with an integrating over an oscillation period, one can obtain following relations:

$$k_{\text{int}} = \frac{F}{A}\sin\theta + m\omega^2 - k, \tag{2.6}$$

$$b_{\text{int}} = \frac{F}{A\omega}\cos\theta - b, \tag{2.7}$$

Note that trigonometrical functions in Eq.(2.6), (2.7) is changed when trigonometrical functions trial solutions in Eq.(2.5) or driven force in Eq.(2.3) is changed.

Figure 2.4 is an example of transformation from electric amplitude (A_e) and phase (θ_e) data to elasticity (k_{int}) and damping (b_{int}). First step, electric amplitude and phase signal is converted to mechanical amplitude (A_m) and phase signal (θ_m) using Eq. (2.1) and 2.2 in Fig. 2.4 (a), (b) (If you used the SCC with TP-QTF system, skip this step.). Here notify that the phase signal (θ_e, θ_m) include the phase shift (δ_e, δ_m) by driven frequency. namely, when oscillator is driven by off-resonance frequency, the phase signal (θ_e, θ_m) is not 0. In fig. 2.4 (b), the black dot line is the electric phase signal (has not 0) of free oscillation, where resonance frequency of QTF is ∼32429.86 Hz and QTF

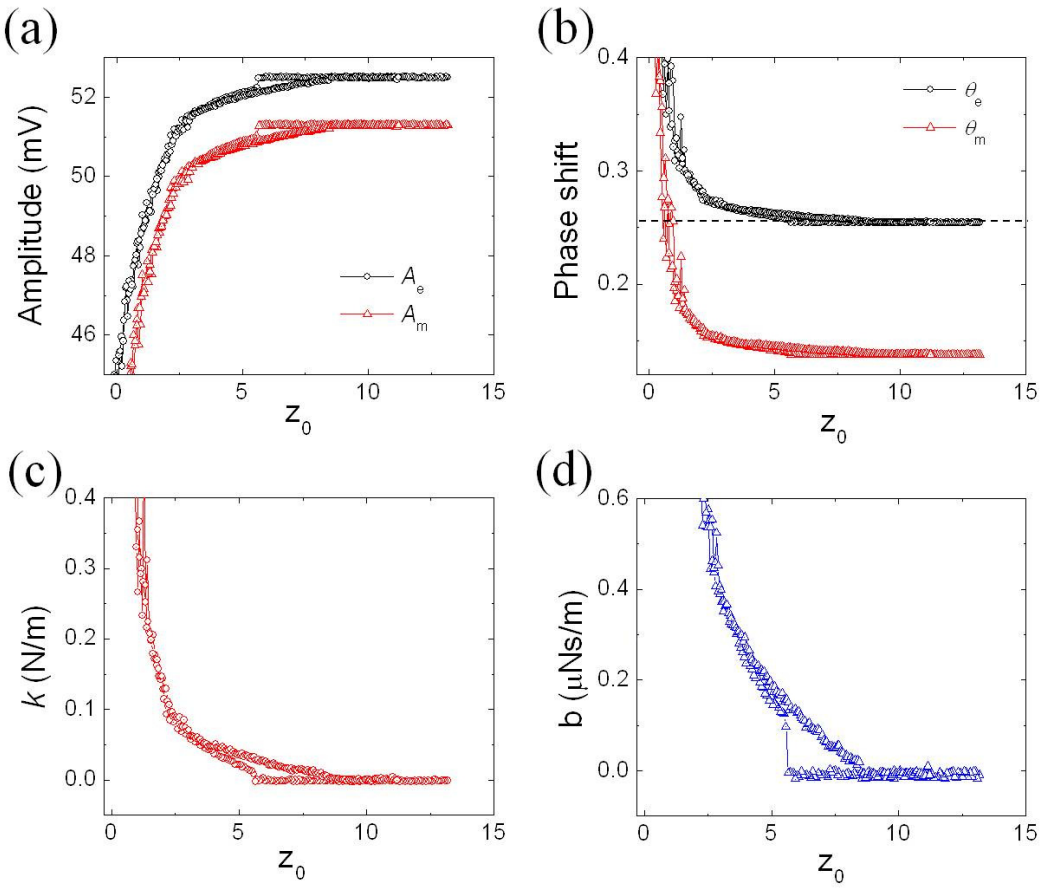

Figure 2.4: Converting data to mechanical values (a), (b) the electrical signals could change to mechanical signals, removed the effective of additive capacitance, using Eq. (2.1) and (2.2). (c), (d) the mechanical signals could convert to effective elasticity and damping by interactive materials using Eq. (2.6) and (2.7)

driven by 32429.5 Hz. Second step, The elasticity (k_{int}) and damping (b_{int}) are obtained by Eq. (2.6), (2.6) using converted A_m, θ_m.

Bibliography

[1] F. J. Giessible, Rev. Mod. Phys. **75**, 949 (2003).

[2] W. J. Y. Seo and C. Hwang, Apply. Phys. Lett. **80**, 4324 (2002).

[3] S. Hembacher, F. J. Giessibe, and J. Mannhart, Science **305**, 380 (2004).

[4] N. Maeda, J. N. Israelachvili, and M. M. Kohonen, Phys. Natl. Acad. Sci. USA **100**, 803 (2003).

[5] M. Lee, J. Jahng, K. Kim, and W. Jhe, Appl. Phys. Lett. **91**, 023117 (2007).

[6] S. An, K. Lee, B. Kim, J. Kim, S. Kwon, Q. Kim, M. Lee, and W. Jhe, Curr. Appl. Phys. **13**, 1899 (2008).

[7] J. Zelenka *Piezoelectric Resonators and their Applications*, (Elsevier, New York, 1986)

[8] M. Lee, B. Sung, N. Hashemi, and W. Jhe, Faraday Discuss. **141**, 415-421 (2009).

[9] S. An, J. Kim, K. Lee, B. Kim, M. Lee, and W. Jhe, Appl. Phys. Lett. **101**, 053114 (2012).

Chapter 3

Mechanical Characteristics of Confined Hydration Water Layer

3.1 Introduction

In nature, the hydration water layer (HWL) where water molecules are tightly bounded to ions or hydrophilic surfaces exists ubiquitously in ambient condition or aqueous solutions. It plays an important role to biological processes [1], abiotic materials process [3], colloidal interaction [4], and friction [6]. Bio materials are mostly covered hydrophilic molecules such as lipid bilayer. Therefore dynamics of HWL is believed to signify to physiological functions, and has been studied by experiments [5] and computer simulation [1]. Sometimes, the mechanism in abiotic materials is also significantly considered HWL. For example, HWL is concerned in Cement setting and cohesion which are major process in

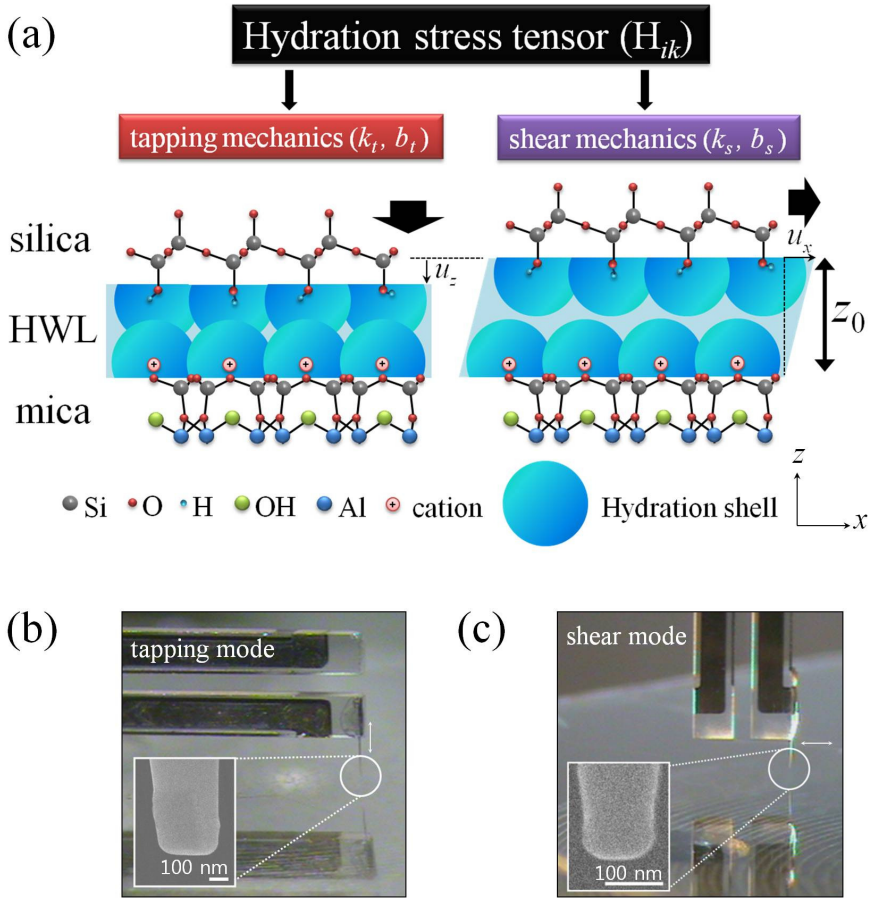

Figure 3.1: (a) schematic diagram for tapping and shear mechanics of hydration water layer(HWL) between mica silica and mica. Elasticity and damping of HWL via tapping and shear mechanics could be driven by Hydration stress tensor. $u_i = x_i' - x_i$ (x_i' and x_i are the position vector after and before deformation) (b), (c) Tapping and shear mode of QTF. The tip of the tapping mode oscillates vertically to the mica surface, and the one of the shear mode oscillates parallel to the mica surface. (inset: scanning electron microscope image of the tip, scale bar is 100 nm)

reinforce concrete structure [3]. In addition, HWL is discreetly researched for hybridization between bio and abiotic materials [2]. Therefore understanding of HWL is significant to realize various natural phenomena, and to develop the technology.

Especially, the characteristic of confined HWL between hydrophilic surfaces are studied by various experiments [6–12] and computer simulations [13, 14]. The hydration force which is the interfacial short range force by HWL is empirically known that decays exponentially with the distance under 1-3 nm gap between hydrophilic surfaces [14, 15]. Moreover, it is observed that HWL has elastic [8, 11, 12], highly viscous [6, 8–10, 12], nonlinear viscoelasticity [11], sluggish relaxation time [8, 11] and non-squeezed fluidity [6, 12] by surface force apparatus (SFA) [8], surface force balance (SFB) [6], and scanning probe microscopy (SPM) [9–12]. Several characteristics of these, sluggish relaxation time, enhanced relaxation time and nonlinear viscoelasticity, was adduced to explain the supercooled liquidity of confined HWL [11, 16]. However the understanding of HWL is still insufficient thus it results in that the viscous and elastic properties of HWL are separately studied without exact relation with each other.

In this chapter, we develop the hydration stress tensor (H_{ik}) based on hydration force which include tapping and shear mechanics, in Fig. 3.1 (a). Then validity of H_{ik} is demonstrated by elastic and viscous response of small tapping and shear deformation of HWL using quartz tuning-fork (QTF) based amplitude modulation (AM) AFM in Fig. 3.1 (b), (c). H_{ik} presents the relation of elastic and viscous properties between tapping and shear mechanism. Moreover, the

measured physical properties show confined HWL has the supercooled liquidity through viscosity ratio (Volume viscosity over dynamic viscosity. Especially it is obtained by relation between tapping and shear mechanics), enhanced dynamic viscosity and sluggish relaxation time.

In This experiments, the flattened silica tip which is fabricated by a mechanical puller (P-2000, Sutter Instruments Co.) and by gently contacting the round tip onto the mica surface in insets of Fig. 3.1(b) and (c). The silica tip is glued to one prong of the QTF has high stiffness (∼20,000 N/m) and quality factor (∼10,000) at the resonant frequency (∼32 kHz) in ambient conditions and it is driven with small oscillation (∼0.2 nm of free oscillation amplitude) [17–19]. The tape-cleaved mica substrate was cleaned by chemical cleansing process with diluted acid [19]. Such a calibrated AM-AFM was placed in a humidity control chamber. All the experiments were performed at room temperature and at a relative humidity of about 80%. The hydrophilic silica and mica are naturally covered by HWL in ambient condition via absorbed water molecules onto surfaces, and the gap (z_0) between silica and mica is filled water by capillary condensation within a low nanometer gap [19]. This water and HWL were used for experiments. Figure 3.1(b), (c) are pictures of QTF for tapping mode (Fig. 3.1(b)) and shear mode (Fig. 3.1(c)). Figure 3.2 shows the elasticity and damping (damping coefficient) of confined water versus the distance between silica tip and mica surface (z_0) for taping [20] (Fig. 3.2(a)) and shear mode [19] (Fig. 3.2(b)). The contact point (z_c) of taping mode and shear mode are determined as the position where damping of tapping mode be-

comes huge noisy in Fig. 3.2(a), and damping of shear mode starts decreasing in Fig. 3.2(b) as the tip approaches the substrate. We decide the distance between surfaces at z_c is 0.3 nm on the assumption that the water molecular monolayer does not squeeze out.

3.2 Development of Hydration Stress Tensor

H_{ik} is derived by two assumptions. (i) Empirically well-known hydration force applied to between surfaces via HWL results from viscoelasticity of HWL, thus it is viscoelastic force rather than static force. (ii) The relation between stress and deformation of HWL complies with well-established theory of elasticity [21] and hydrodynamics [22]. Hydration force is known to follow the simple equation [15, 20]:

$$F^{(h)} = \Omega P \mathrm{e}^{-z_0/\lambda_0} \tag{3.1}$$

where Ω is the interacting area, and P, λ_0 are constants. Originally, the hydration force Eq. (3.1) is not dependent on velocity since most hydration force had measured statically using SFA [15]; therefore, the force does not affect damping. However, first assumption needs the hydration force would be the function of velocity to arise damping in Eq. (3.1) when it is measured dynamically. Clearly, Ω is a constant, whereas the pressure by HWL at z_0 ($P\mathrm{e}^{-z_0/\lambda_0}$) is results from viscoelasticity of HWL then it could be influenced by velocity. If deformation is enough small λ_0, which decides the whole shape of the force, it is not influenced by the local deformation. Therefore, the P would be the function of the velocity,

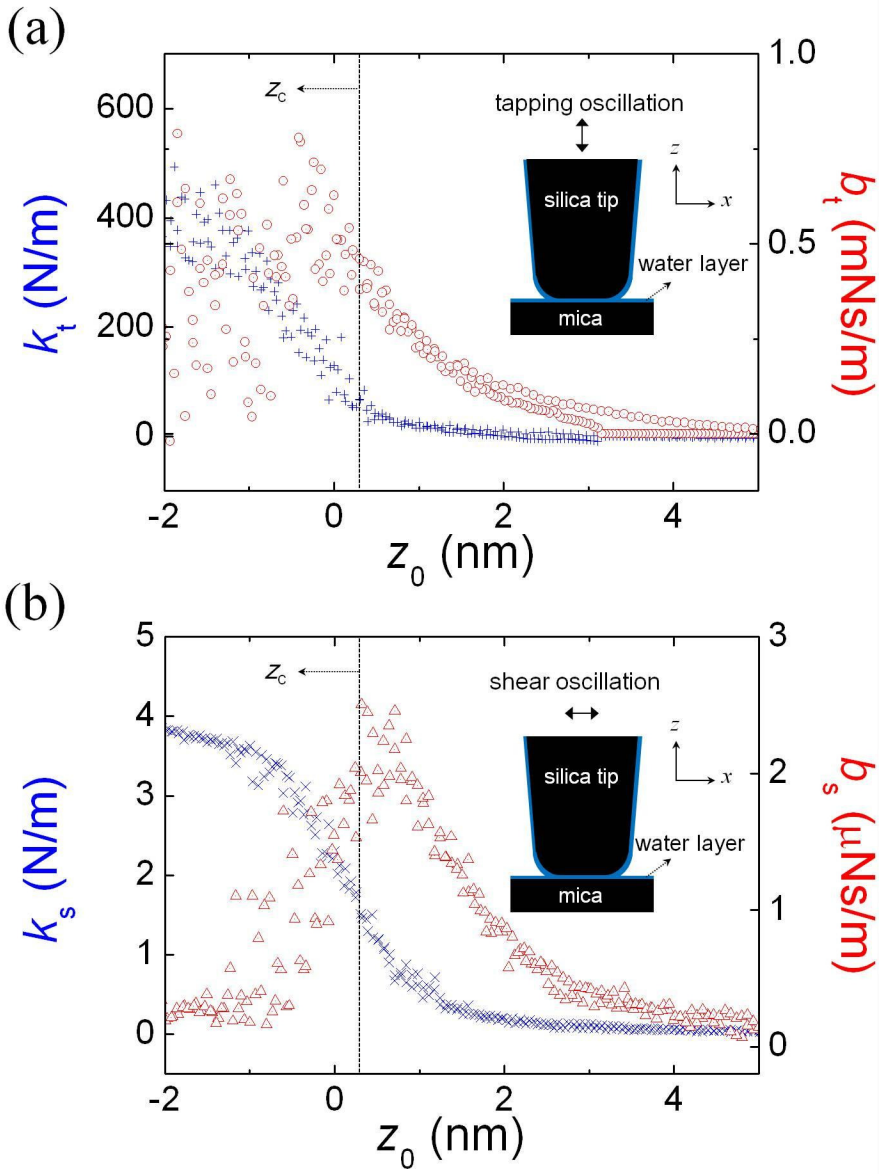

Figure 3.2: Measured elasticity and damping on (a) tapping and (b) shear mode. The contact point (z_c) of taping mode is determined as the position where damping of becomes huge noisy, and shear mode is decided the position where damping starts decreasing as the tip approaches the substrate. We appoint z_c is 0.3 nm on the assumption where the water molecular monolayer exists.

and could be expanded with the Taylor series in the case of small deformation:

$$P(v) \approx P_0 + \left.\frac{\mathrm{d}P_0}{\mathrm{d}v}\right|_0 v \equiv \left(1 - \frac{v}{\nu_0}\right) P_0 \tag{3.2}$$

where $P_0 = P(0)$, $\frac{1}{\nu_0} \equiv \frac{-1}{P_0} \left.\frac{\mathrm{d}P_0}{\mathrm{d}v}\right|_0$, and ν_0 is constant. By inserting Eq. (3.2) into Eq. (3.1), and $z\,(= z_0 + \Delta z)$ into z_0, one can obtain the following force:

$$F^{(h)}(z, \dot{z}) = \Omega_t P_0 \left(1 - \frac{v}{\nu_0}\right) \mathrm{e}^{-z/\lambda_0}. \tag{3.3}$$

Generally any force can be also expanded with the Taylor series:

$$\begin{aligned} F(z_0 + \Delta z, \dot{z}_0 + \Delta \dot{z}) &\approx F(z_0, \dot{z}_0) + \frac{\partial F}{\partial z}\Delta z + \frac{\partial F}{\partial \dot{z}}\Delta \dot{z} \\ &\equiv F(z_0, \dot{z}_0) - k\Delta z - b\Delta \dot{z}. \end{aligned} \tag{3.4}$$

Inserting Eq.(3.3) into into Eq.(3.4) then k and b is obtained as follow:

$$\begin{aligned} k_t^{(h)} &= \Omega \frac{P_0}{\lambda_0} \mathrm{e}^{-z_0/\lambda_0}, \\ b_t^{(h)} &= \Omega \frac{P_0}{\nu_0} \mathrm{e}^{-z_0/\lambda_0}, \end{aligned} \tag{3.5}$$

where $k_t^{(h)}$ and $b_t^{(h)}$ mean the elasticity and damping via HWL by tapping deformation. Even though deformation is focused on the harmonic motion for comparable AFM experiments, the results coincide. To check, let the solutions are as:

$$\begin{aligned} z &= z_0 + A_t \sin\left[\omega t + \theta\right], \\ v &= A_t \omega \cos\left[\omega t + \theta\right]. \end{aligned} \tag{3.6}$$

where A_t is the amplitude of oscillating motion. Inserting Eq. (3.3) and (3.6) into Eq. (3.4) and multiplying both sides of the resulting equation by $\sin\left[\omega t + \theta\right]$

and $\cos[\omega t + \theta]$, with an integrating over an oscillation period, one can obtain following relations:

$$k_t^{(h)}(z_0) = \frac{2I_1(A_t/\lambda_0)}{A_t} F^{(h)}(z_0, 0) \approx \Omega \frac{P_0}{\lambda_0} \mathrm{e}^{-z_0/\lambda_0}, \tag{3.7}$$

$$b_t^{(h)}(z_0) = \frac{2\lambda_0 I_1(A_t/\lambda_0)}{\nu_0 A_t} F^{(h)}(z_0, 0) \approx \Omega \frac{P_0}{\nu_0} \mathrm{e}^{-z_0/\lambda_0}, \tag{3.8}$$

where $I_1(A_t/\lambda_0)$ is the first-order modified Bessel function. When A_t is enough smaller than λ_0, $I_1(A_t/\lambda_0)$ becomes approximately $A_t/(2\lambda_0)$. Note that the $k_t^{(h)}$ and $b_t^{(h)}$ of Eq. (3.7) and (3.8) coincides with Eq. (3.5).

Next we could transform $k_t^{(h)}$ and $b_t^{(h)}$ to shear elasticity($k_s^{(h)}$) and damping ($b_s^{(h)}$) through relation of stress-strain in theory of elasticity [21] and stress-strain rate in hydrodynamics [22] by second assumption. In theory of elasticity, strain tensor is given by [21]:

$$\gamma_{ik} = \frac{1}{2}\left(\frac{\partial u_i}{\partial x_k} + \frac{\partial u_k}{\partial x_i}\right) \tag{3.9}$$

in small deformation, where and x_i is the position vector in space (x, y, z) and $u_i = x_i' - x_i$ (x_i' and x_i are the position vector after and before deformation). The stress tensor (σ_{ik}) is given in theory of elasticity as follow:

$$\sigma_{ik} = \frac{E}{1+\sigma}\left(\gamma_{ik} + \frac{\sigma}{1-2\sigma}\gamma_{ll}\delta_{ik}\right) \tag{3.10}$$

where E is Young's modulus, σ Poisson's ratio and δ_{ik} Kronecker delta function. The stress by tapping deformation is expressed as $\sigma_{zz} = E\gamma_{zz}(1-\sigma)/[(1+\sigma)(1-2\sigma)]$ with $\sigma_{xx} = \sigma_{yy} = 0$ while stress is also expressed as elastic force via deformed HWL per the interacting area as $k_t^{(h)} u_z/\Omega$. And if strain is linear ($\gamma_{zz} =$

$u_z(z_0)/z_0$), Young's modulus could be obtained by (Note that we concern only the stress by small deformation at z_0):

$$E = \frac{P_0 z_0}{\lambda_0} \mathrm{e}^{-z_0/\lambda_0} \frac{(1+\sigma)(1-2\sigma)}{(1-\sigma)}. \tag{3.11}$$

Inserting Eq. (3.11) into (3.10) then shear stress is obtained by:

$$\sigma_{zx} = \frac{P_0 z_0}{\lambda_0} e^{-z_0/\lambda_0} \frac{(1-2\sigma)}{(1-\sigma)} \gamma_{zx}, \tag{3.12}$$

while the shear stress also described by $k_s^{(h)} u_x/\Omega$ similar with normal stress. If shear strain γ_{zx} is linear as $u_x(z_0)/z_0$, $k_s^{(h)}$ is as follow:

$$k_s^{(h)} = \frac{\Omega P_0}{\lambda_0} \mathrm{e}^{-z_0/\lambda_0} \frac{(1-2\sigma)}{(1-\sigma)}. \tag{3.13}$$

In hydrodynamics the stress tensor (σ'_{ik}) is given as follow [22]:

$$\sigma'_{ik} = \eta \left(\frac{\partial v_i}{\partial x_k} + \frac{\partial v_k}{\partial x_i} - \frac{2}{3} \frac{\partial v_l}{\partial x_l} \delta_{ik} \right) + \zeta \frac{\partial v_l}{\partial x_l} \delta_{ik} \tag{3.14}$$

where η is dynamic viscosity, ζ volume viscosity and v_i velocity vector of flow. When fluid is incompressible, divergence of velocity is zero ($\partial v_l/\partial x_l = 0$) by the equation of continuity [22]. However HWL is not well squeeze out [6,12] and the water molecules are bounded tightly on the surfaces [6] thus we should consider the divergence term. The normal stress in hydrodynamics is follows:

$$\sigma'_{zz} = \frac{4}{3}\eta \frac{\partial v_z}{\partial z} + \zeta \frac{\partial v_z}{\partial z} = \eta \left(\frac{4}{3} + \alpha \right) \frac{\partial v_z}{\partial z} \tag{3.15}$$

where α is the viscosity ratio (ζ/η). Notice that we put the divergence of velocity is $\partial v_z/\partial z$ since HWL is difficult to squeeze out [6, 12]. Stress also presents

damping force via HWL per the interacting area as $b_t^{(h)} v_z/\Omega$. Then we could obtain viscosity as:

$$\eta = \frac{P_0 z_0}{\nu_0} \mathrm{e}^{-z_0/\lambda_0} \left(\frac{4}{3} + \alpha\right)^{-1}. \tag{3.16}$$

Inserting Eq. 3.16 into 3.15 then shear stress is obtained by:

$$\sigma'_{zx} = \frac{P_0 z_0}{\nu_0} \mathrm{e}^{-z_0/\lambda_0} \left(\frac{4}{3} + \alpha\right)^{-1} \frac{\partial v_x}{\partial z} \tag{3.17}$$

and shear stress also described as $b_s^{(h)} v_x/\Omega$. If velocity gradient is linear as $v_x\left(z_0\right)/z_0$, $b_s^{(h)}$ is as follows:

$$b_s^{(h)} = \frac{\Omega_s P_0}{\nu_0} \mathrm{e}^{-z_0/\lambda_0} \left(\frac{4}{3} + \alpha\right)^{-1}. \tag{3.18}$$

Finally, hydration stress tensor (H_{ik}) could be obtained by summation stress tensors ($\sigma_{ik} + \sigma'_{ik}$) with Young's modulus (Eq. 3.11) and viscosity (Eq. 3.15) of HWL as follows:

$$\begin{aligned} H_{ik} = P_0 z_0 \mathrm{e}^{-z_0/\lambda_0} \Bigg[& \frac{1-2\sigma}{\lambda_0\left(1-\sigma\right)} \left(\gamma_{ik} + \frac{\sigma \gamma_{ll} \delta_{ik}}{1-2\sigma}\right) \\ & + \frac{1}{\nu_0} \left(\frac{4}{3} + \alpha\right)^{-1} \left(2\dot{\gamma}_{ik} + \left(\frac{-2}{3} + \alpha\right) \dot{\gamma}_{ll} \delta_{ik}\right) \Bigg]. \end{aligned} \tag{3.19}$$

Here $\dot{\gamma}_{ik}$ is the strain rate which is obtained by time derivative of the strain, $\dot{\gamma}_{ik} = \partial \gamma_{ik}/\partial t$. Equation (16) is our main result that represents the unified expression of the the hydration stress tensor H_{ik}. Notice that the tapping and shear component of H_{ik} (H_{zz}, H_{zx}) provide the elasticity ($k_t^{(h)}$, $k_s^{(h)}$) and damping coefficient ($b_t^{(h)}$, $b_s^{(h)}$), respectively, identical to Eqs. (3.5), (3.13) and (3.18),

$$H_{zz} = \frac{k_t^{(h)}}{\Omega} u_z + \frac{b_t^{(h)}}{\Omega} v_z \,, \tag{3.20}$$

$$H_{zx} = \frac{k_s^{(h)}}{\Omega} u_x + \frac{b_s^{(h)}}{\Omega} v_x \ . \tag{3.21}$$

3.3 Validity of Hydration Stress Tensor using QTF-AFM

In Fig. 3.3, the expected elastic (Eq. 3.7) and damping (Eq. 3.8) values are compared with tapping mode AFM results with various tips had each diameter. Measured data under 2.5 nm agrees with $k_t^{(h)}$, $b_t^{(h)}$ where P_0, λ_0 and ν_0 are about 1.9±0.5 MPa, 1.4±0.4 nm and $(1.1 \pm 0.4)\times 10^{-4}$ m/s. In Fig. 3.3 and 3.4, the area between dotted lines is the error region of the expected value by H_{ik} of upper limitation and bottom limitation. The error limitation is decided by error of radius of interacting area and contact point. The error of contact point is given to ±0.3 nm.

Figure 3.4 shows the comparison between expected elastic (Eq. 3.13) and damping (Eq. 3.18) values and shear mode AFM results with various tips which tips are differnt with tapping tips. In shear experiment, we could obtain Poisson's ratio ($\sigma \sim 0.3 \pm 0.1$) and viscosity ratio ($\alpha \sim 10 \pm 3$) through data fitting. And directly we could transform elastic (k_h) and damping (b_h) data to shear modulus ($G = k_s z_0/\Omega$, in Fig. 3.5(a)) and dynamic viscosity ($\eta = b_s z_0/\Omega$, in Fig. 3.5(b)). By recent reports, confined HWL has similar characteristics with supercooled water such as enhancement viscosity and sluggish relaxation time [11,16]. Our results also agree with supercooled liquidity of HWL by three aspects. (i)

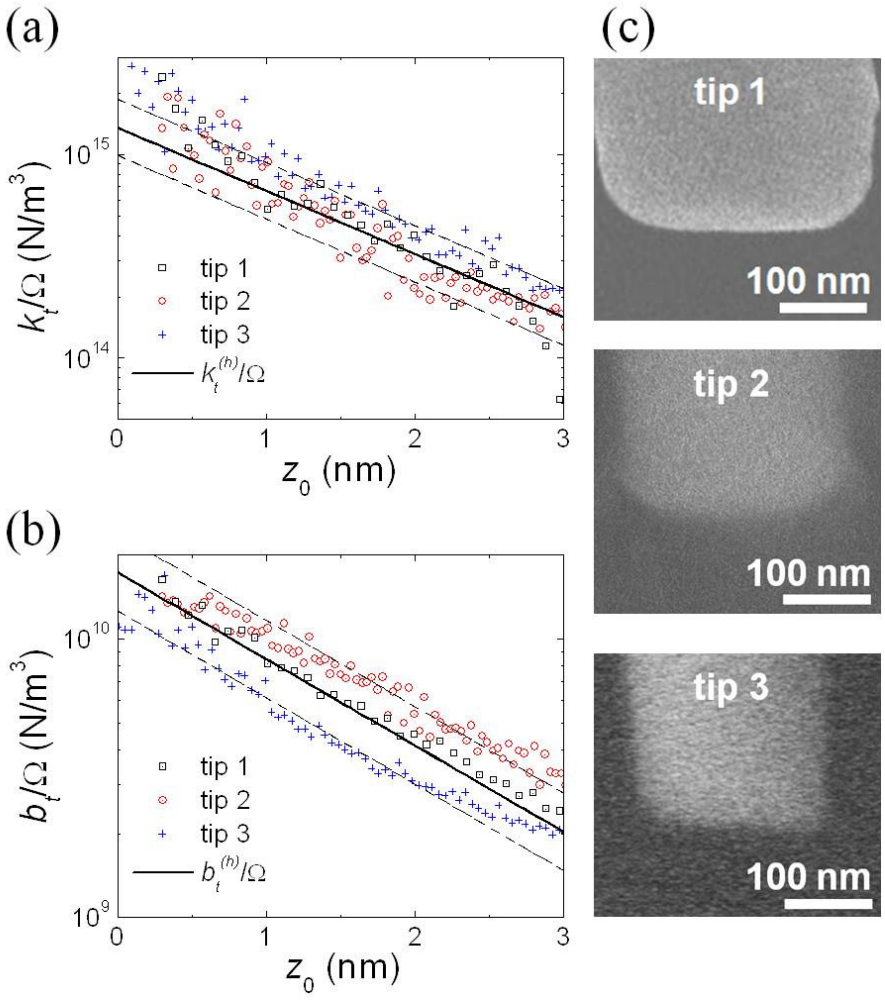

Figure 3.3: Tapping mechanics. (a) Elasticity and (b) damping versus z_0 under 3 nm on tapping mode. The data (k_t, b_t) is fitted by Eq. (3.7) and (3.8) ($k_t^{(h)}$, $b_t^{(h)}$). The area between dotted lines is the error region of the calculated value ($k_t^{(h)}$, $b_t^{(h)}$). The radius (r_c) of interacting area of tip and contact point (z_c) result in error area. (c) various silica tips used tapping experiments. (The flatten area radii of tip 1, tip 2, tip 3 are 95±5, 75±5, 80±5 nm, respectively.)

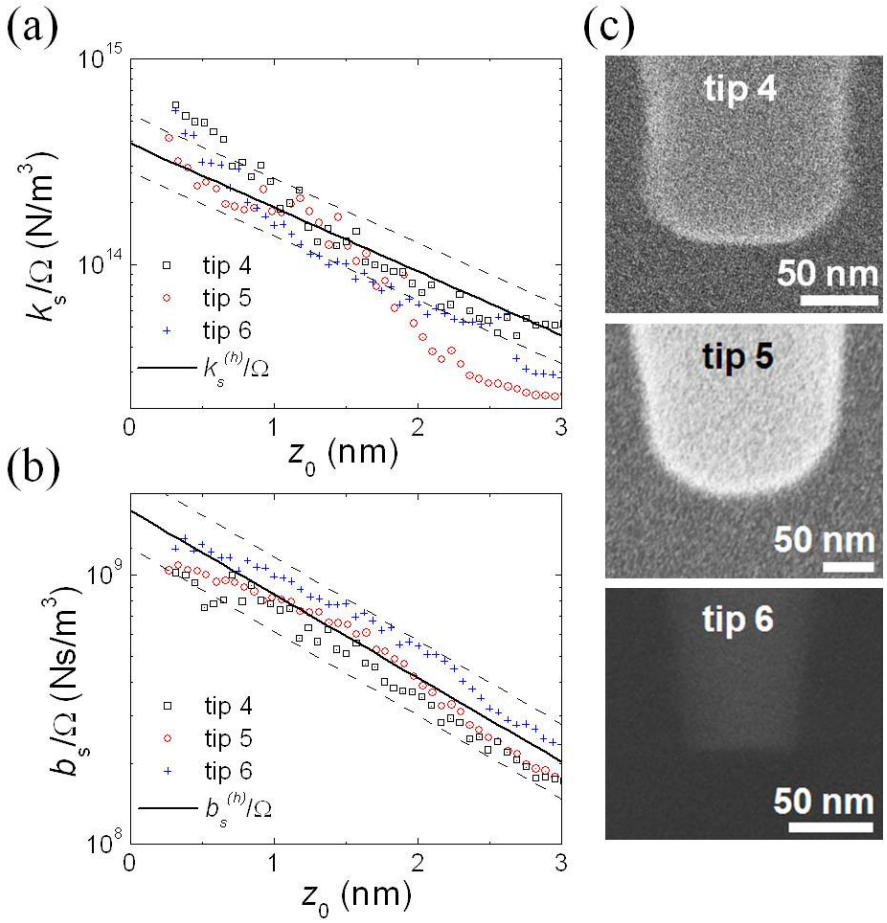

Figure 3.4: Shear mechanics. (a) Elasticity (inset: shear modulus $k_s u_x/\Omega_s$) and (b) damping (inset: dynamic viscosity $b_s u_x/\Omega_s$) versus z_0 under 3 nm on shear mode. The data (k_s, b_s) is fitted by Eq. (3.13) and (3.18) ($k_s^{(h)}$, $b_s^{(h)}$). The area between dotted lines is the error region of the calculated value ($k_s^{(h)}, b_s^{(h)}$). The radius (r_c) of interacting area of tip and contact point (z_c) result in error area. (c) various silica tips used tapping experiments. (The flatten area radii of tip 4, tip 5, tip 6 are 28±2.5, 32±2.5, 30±2.5 nm, respectively.)

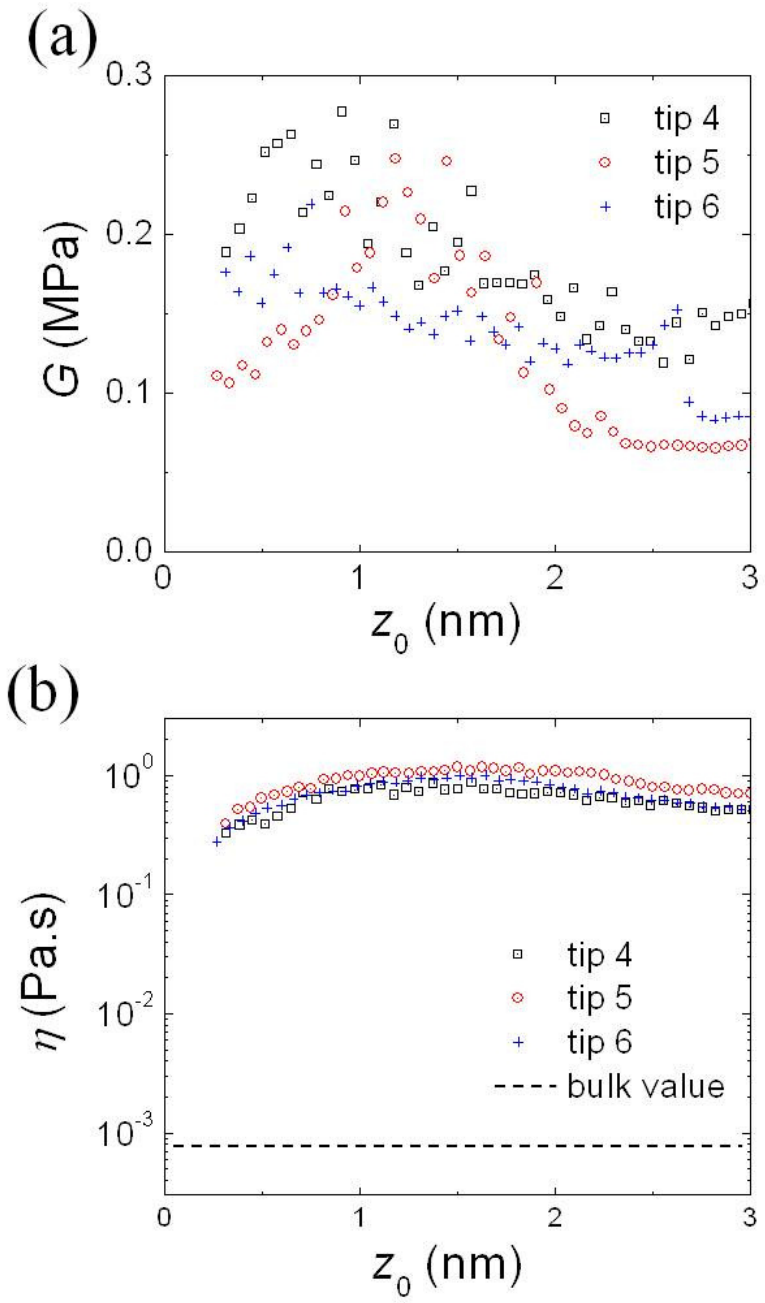

Figure 3.5: (a) shear modulus directly obtained by shear elasticity. the value is similar with soft materials shch as cell or rubber. (b) shear viscosity obtained by shear damping coefficient. The viscosity is about 1000 times larger than bulk shear viscosity.

The measured viscosity is increase about 1,000 times compared with bulk water. (ii) The dynamic relaxation time by Maxwell model ($G/(\eta\omega) \sim 1$ μm) is longer than bulk water (~ 1 ps) [23]. (iii) The viscosity ratio is larger than bulk water. The viscosity ratio increases with decreasing the temperature and does not overcome about 4 over the freezing temperature (0 °C) [24]. Therefore the viscosity ratio of supercooled water may be expected is larger than 4. Elastic properties of HWL are difficult to compare with supercooled water due to lack of experimental reports.

Emphatic point is Poisson's ratio (σ) and viscosity ratio (ζ/η) are additionally obtained by relations between ($k_t^{(h)}$, $b_t^{(h)}$) and ($k_s^{(h)}$, $b_s^{(h)}$) which could be also derived by H_{ik}. Most solid materials have Poisson's ratio, which means compressibility of material, values between $0 \sim 0.5$. Poisson's ratio of the perfectly incompressible material such as rubber is 0.5 while regular steels has about 0.3 value [25]. The volume viscosity also means compressibility of fluids. We could obtained volume viscosity to multiply α and dynamic viscosity ($b_s z_0/\Omega$) about 10 Pa·s which is 4,000 times larger than bulk water driven by MHz [24].

3.4 Conclusion

In conclusion, we have derived the hydration stress tensor (H_{ik}) and demonstrated its validity through tapping and shear mode AFM experiments. Until now, tapping, shear dynamical properties of confined HWL had individually studied. However, if the measured quantities are results from the responses of

HWL, the relation between the quantities should exist. Through this study, It is shown that the dynamical properties of confined HWL are related by H_{ik}, and Poisson's ratio and volume viscosity could be obtained by relations between tapping and shear dynamic properties. This results may contribute to study of natural phenomena and development of technology where mechanism of HWL is important, such as bio molecules, colloidal particles, MEMS system, *etc.*

Bibliography

[1] Y. Hansen, S. Gekle, and R. Netz, Phys. Rev. Lett. **111**, 118103 (2013).

[2] X. Qiu, C. Khripin, F. Ke, S. Howell, and M. Zheng, Phys. Rev. Lett. **111**, 048301 (2013).

[3] E. Masoero, E. Del Gado, R. J.-M. Pellenq, F.-J. Ulm, S. Yip, Phys. Rev. Lett. **109**, 155503 (2012).

[4] A. Santos and Y. Levin, Phys. Rev. Lett. **106**, 167801 (2011).

[5] M. Hishida and K. Tanaka, Phys. Rev. Lett. **106**, 158102 (2011).

[6] U. Raviv and J. Klein, Science **297**, 1540 (2002).

[7] J. Israelachvili and H. Wennerström, Nature **219**, 379 (1996).

[8] Y. Zhu and S. Granick, Phys. Rev. Lett. **87**, 096104 (2001).

[9] R. C. Major, J. E. Houston,d M. J. McGrath, J. I. Siepmann, and X.-Y. Zhu, Phys. Rev. Lett. **96**, 177803 (2006).

[10] T. Li and J. Gao and R. Szoszkiewicz and U. Landman and and E. Riedo, Phys. Rev. B **75**, 115415 (2007).

[11] T. Li and E. Riedo, Phys. Rev. Lett. **100**, 106102 (2008).

[12] S. Khan, G. Matei, S. Patil, and P. Hoffmann, Phys. Rev. Lett. **105**, 106101 (2010).

[13] Y. Leng and P. Phys. Rev. Lett. **94**, 026101 (2005).

[14] J. Faraudo and F. Bresme, Phys. Rev. Lett. **94**, 077802 (2005).

[15] J. N. Israelachvili *Inatermolecular and surface forces 3rd edi.* (Elsevier Press, 2011).

[16] S. Granick, S. Bae, S. Kumar, and C. Yu, Physics **3**, 73 (2010).

[17] F. Giessibl, Appl. Phys. Letts. **73**, 3956 (1998).

[18] M. Lee, J. Jahng, K. Kim, and W. Jhe, Appl. Phys. Lett. **73**, 023117 (2007).

[19] M. Lee, B. Sung, N. Hashemi, and W. Jhe, Faraday Discuss.**141**, 415 (2009).

[20] M. Lee and W. Jhe, Phys. Rev. Lett. **97**, 036104 (2006).

[21] L. D. Landau and E. M. Lifshitz *Theory of Elasticity 3rd edi.* (Elsevier Press, 2008).

[22] L. D. Landau and E. M. Lifshitz *Fluid Mechanics 2nd edi.* (Elsevier Press, 2007).

[23] N. Micali, S. Trusso, C. Vasi, D. Blaudez, and F. Mallamace, Phys. Rev. E 141, **54**, 1720 (1996).

[24] M. J. Holmes, N. G. Parker, and M. J. W. Povey, J. Phys.: Conf. Ser. **269**, 012011 (2011).

[25] F. Cardarelli *Materials Handbook* (Springer Press, 2008).

Chapter 4

Nanoscale Turbulence in Confined HWL

4.1 Introduction

Flows at high Reynolds number (Re) above $\sim 10^3$, typically corresponding to large systems, become turbulent, whereas low Re flows are laminar. However, the laminar-turbulent transition occurs at low Re (<1) if with sufficient elasticity, called elastic turbulence (ET), such as in mm-sized viscoelastic fluids [1–7]. The question remains whether extremely small systems, which require too fast flow to reach high Re, exhibit ET. Here we show nanoconfined hydration water layer (HWL) [8] shearing between two hydrophilic surfaces produces ET at vanishing Re ($\sim 10^{-9}$). In NW of variable thickness (0.4 to 1.5 nm), flow resistance increases abruptly above the threshold shear rate $\sim$106 s^{-1} or shear velocity

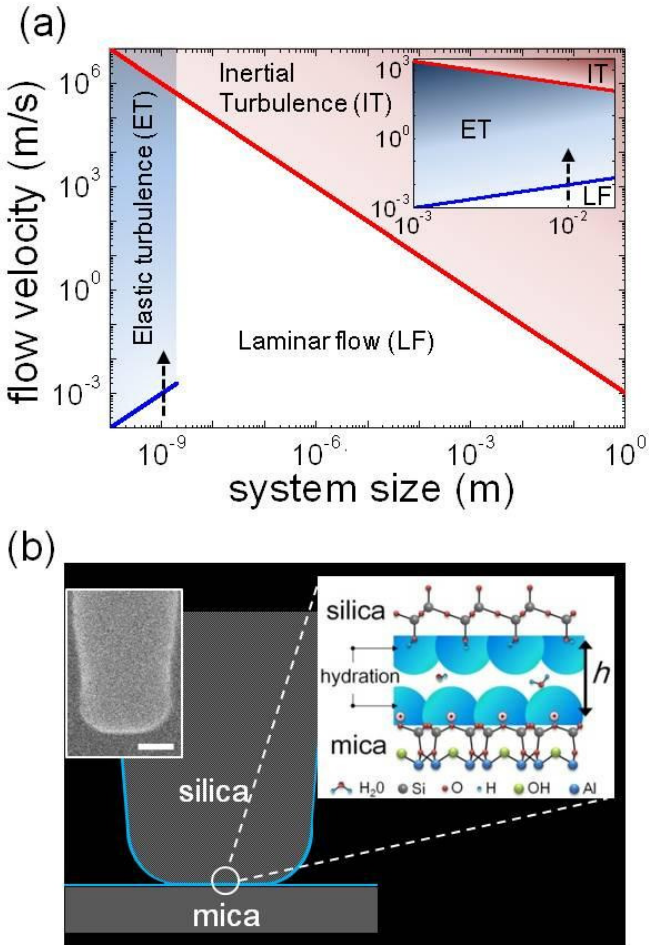

Figure 4.1: Flow phase diagram in viscoelastic liquid. The red line presents the Reynolds number Re=10^3 for bulk water, across which the fluid triggers transition from laminar flow (LF) to inertial turbulence (IT) above a threshold flow velocity at a given system size. The blue line presents the Weissenberg number Wi=1 for viscoelastic liquid had 1μs relaxation time, across which the flow can exhibit elastic turbulence (ET). Notice that, contrary to IT, ET can occur at a low flow velocity in a small system, even in the nonlinearly viscoelastic nanoconfined Hydration water layer (HWL). Inset shows the occurrence of ET for viscoelastic polymer solution, observed at 1 cm system size and 1 mm flow velocity. b, Schematic of experimental system consisting of nanoconfined water layer ($h \approx$ 0.8nm thick) formed between fused silica tip and mica surface in ambient conditions. (Left inset: scanning electron micrograph image of the flattened tip; scale bar is 50 nm).

$\sim 0.7 \pm 0.3$ mm/s. Theoretical analysis indicates ET is attributed to correlation between fluctuations of shear rate and stress. Our results offer fundamental understanding of autoregulation [9–11] in brain capillaries, which maintain slow ($\sim$1 mm/s) and steady (despite blood-pressure change) blood flow, as due to ET in NW between erythrocytes and endothelium.

In Newtonian fluid such as bulk water, turbulence due to inertia force only exists, so-called inertial turbulence (IT). In Fig. 4.1 (a), the red line represents Re $\sim 10^3$ for bulk water where transition from laminar flow (LF) to IT occurs (Re= $\rho vh/\eta$, where ρ, v, h and η are the fluid density, velocity, system size and viscosity, respectively) [12]. Notice that since Re is proportional to system size, smaller system requires higher flow velocity to produce IT. However, polymer solution exhibits ET at much smaller Re, which contributes to realize microfluidic mixing [2,13]. Such LF-to-ET transition is characterized by the Weissenberg number Wi (Wi= $\tau\dot{\gamma} \sim \tau v/h$, where τ and $\dot{\gamma}$ are the fluid relaxation time and shear rate), which is inversely proportional to system size, so that low velocity induces ET even for small systems. For example, polymer solution of 1 cm size and 1 s relaxation time has shown ET at 10 mm/s velocity (see arrow in the inset of Fig. 4.1 (a)).

The question of turbulence at nanoscale is intriguing and challenging. Although IT is impossible for nanoscale water because 10^6 m/s velocity is required (red line in Fig. 4.1 (a)), HWL between two hydrophilic surfaces has intrinsically nonlinear viscoelasticity8 so that ET is possible at much low velocity. For example, for HWL of 1 nm thickness and 1 μs relaxation time, ET occurs at

1 mm/s, which corresponds to 10^6 s^{-1} shear rate. Since it has been difficult to realize HWL of ∼1 nm thickness under high shear rate, ET at nanoscale still remains unexplored. By using noncontact shear-mode atomic force microscopy (AFM) based on quartz tuning fork crystal [14] in ambient condition (Methods), which supports high shear rate, we have addressed ET in NW. Notice that NW above ∼2 nm thickness behaves almost linearly so that ET is not expected (blue line segment in Fig. 4.1 (a)).

4.2 Nonlinear Dynamics of HWL

The AFM measures the viscoelasticity of HWL and its fluid dynamics (Fig. 4.1 (b)) [14]. We have varied the shear rate of the flattened tip, $\dot{\gamma} \approx v_{\rm tip}/h \approx A_{\rm s}\omega/h$. Here, $v_{\rm tip}$ is the tip velocity (ranging from 0.03 to 3 mm/s), $A_{\rm s}$ the tip-oscillation amplitude and $\omega/(2\pi)$ the fixed drive frequency (32 kHz). Figures 4.2 (a), (b), present the measured effective damping coefficient $b_{\rm s}$ and elasticity $k_{\rm s}$, respectively, versus h at various $A_{\rm s}$ [14]. As shown, $b_{\rm s}$ and $k_{\rm s}$ increase rapidly for $h < 2$ nm where the differing amplitude dependence is evident. To address the rheological behaviors of NW, $b_{\rm s}$ and $k_{\rm s}$ in Fig. 4.3 are plotted in terms of the shear viscosity ($\eta = b_{\rm s}h/\Omega$; Ω is the tip-contact area) and shear modulus ($G = k_{\rm s}h/\Omega$) versus $\dot{\gamma}$ in Figs. 4.3 (a), (b), respectively, where one can observe the non-Newtonian fluidity of HWL.

Interestingly, the shear viscosity on the plateau is 300 ∼ 800 times larger than that of bulk water (4.3 (a)), in qualitative agreement with previous results

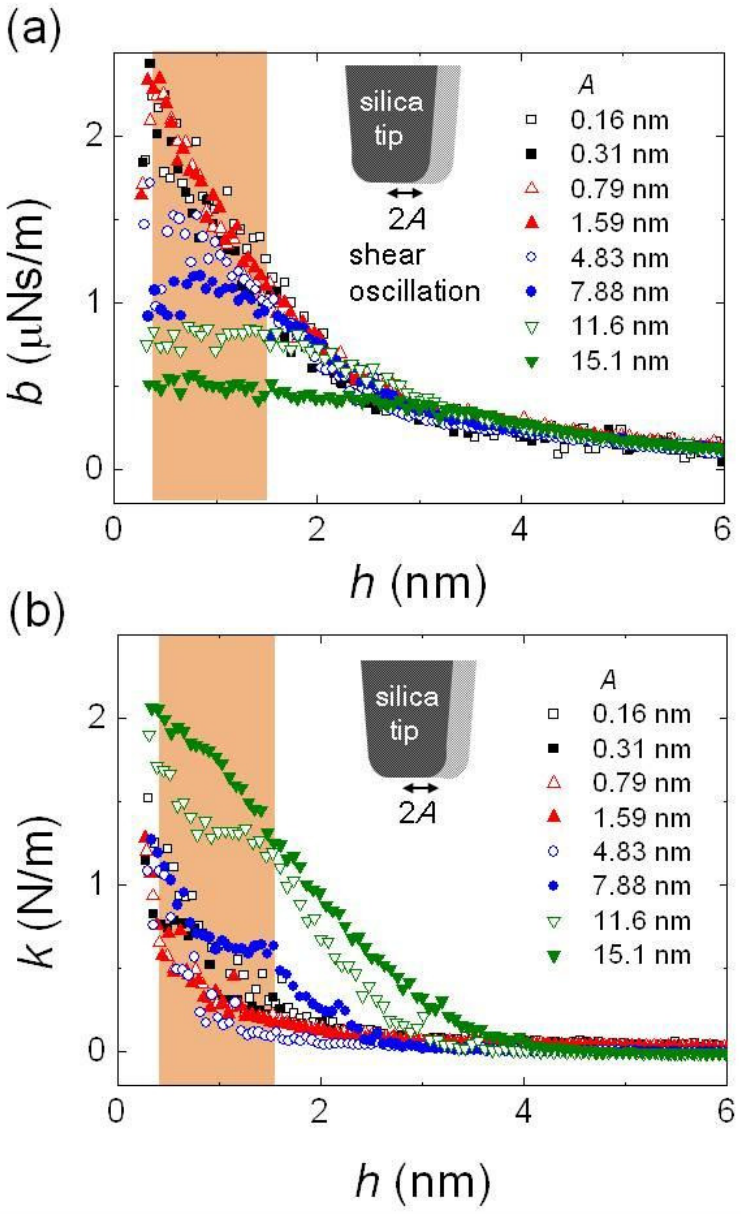

Figure 4.2: Measured shear (a) damping-coefficient and (b) elasticity, respectively, versus the tip-mica distance h at various shear-oscillation amplitude A_s.The colored region of $0.4 \leq h \leq 1.5$ nm indicates that the data used for our viscoelasticity analysis of HWL.

[8, 15], which helps protect the biological cell membranes against mechanical contact damage since it is difficult to squeeze out the trapped HWL. One can also find η sharply decreases above the critical value $\dot{\gamma}_c$, known as shear thinning, from which the shear relaxation-time can be estimated by $\tau \approx 1/\dot{\gamma}_c \approx 10^{-6}$s . Notice that this lies between the calculated [16] ($\sim 10^{-9}$s) and experimental [16] (($\sim 10^{-3}$s) value: the slow relaxation or sluggish dynamics may be attributed to the increased correlation time of hydrogen-bond network in the hydration layers between hydrophilic surfaces [16].

Figure 4.3 (b) shows sharp increase of G, unlike η, above each threshold $\dot{\gamma}_{\rm th}$ that decreases with increasing h. This unexpected but remarkable behaviour suggests the elasticity-induced turbulence or ET [1, 3, 4, 17]. The sharp increase of G clearly demonstrates it accompanies enhancement of both the effective viscosity (or the magnitude of complex viscosity, $|\eta*| = \sqrt{\eta^2 + (G/\omega)^2}$) (Fig. 4.4 (a)) and the stress ratio, $\sigma/\sigma_{\rm LF}$, the measure of turbulent resistance [1]. Here σ is the stress of HWL given by multiplying $|\eta*|$ and $\dot{\gamma}$, while $\sigma_{\rm LF}$ is the stress of LF obtained by fitting the linear region below ET threshold. To address the enhancement of stress associated with ET without inertial term in hydrodynamics, Next chapter Reynolds number (Re) and Weissenberg number (Wi) are presented, and, dynamics of nonlinear Maxwell model is introduced.

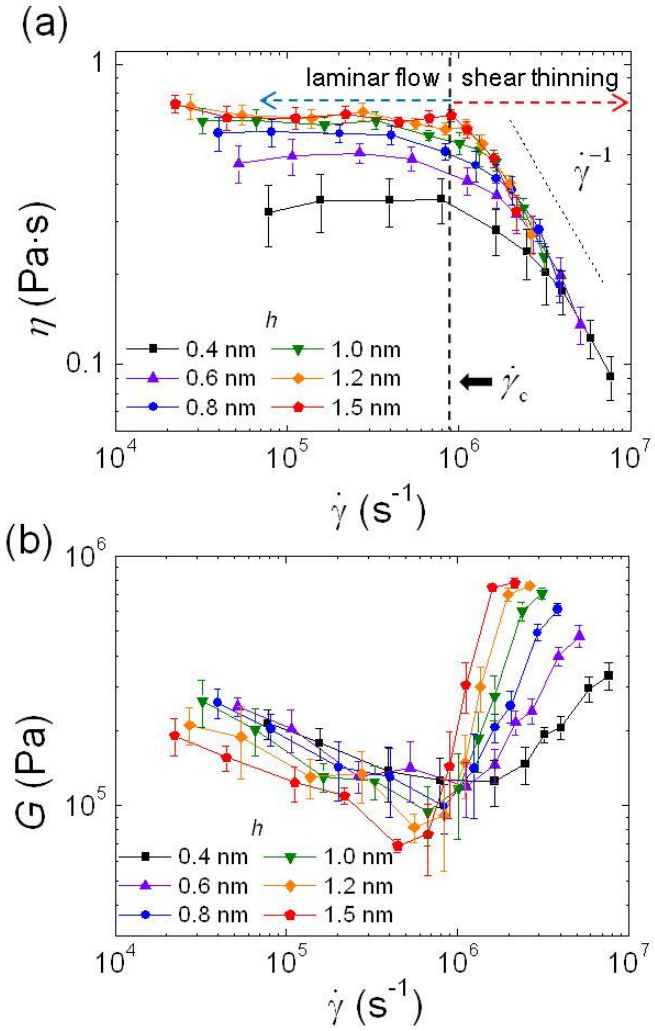

Figure 4.3: (a) Shear viscosity versus shear rate at various h. Shear thinning presented nonlinear fluidity occurs above the threshold shear rate of 10^6 s^{-1}, corresponding to 1 μs relaxation time, which indicates HWL has the nonlinear viscoelasticity. (b), Shear modulus versus shear rate at various h. Shear modulus hugely increases above threshold and the transition occurs at lower threshold for larger h. The results inspires of ET, first observed in viscoelastic polymer solution. Each data point represents average of twelve measurements and its error bars correspond to standard deviation.

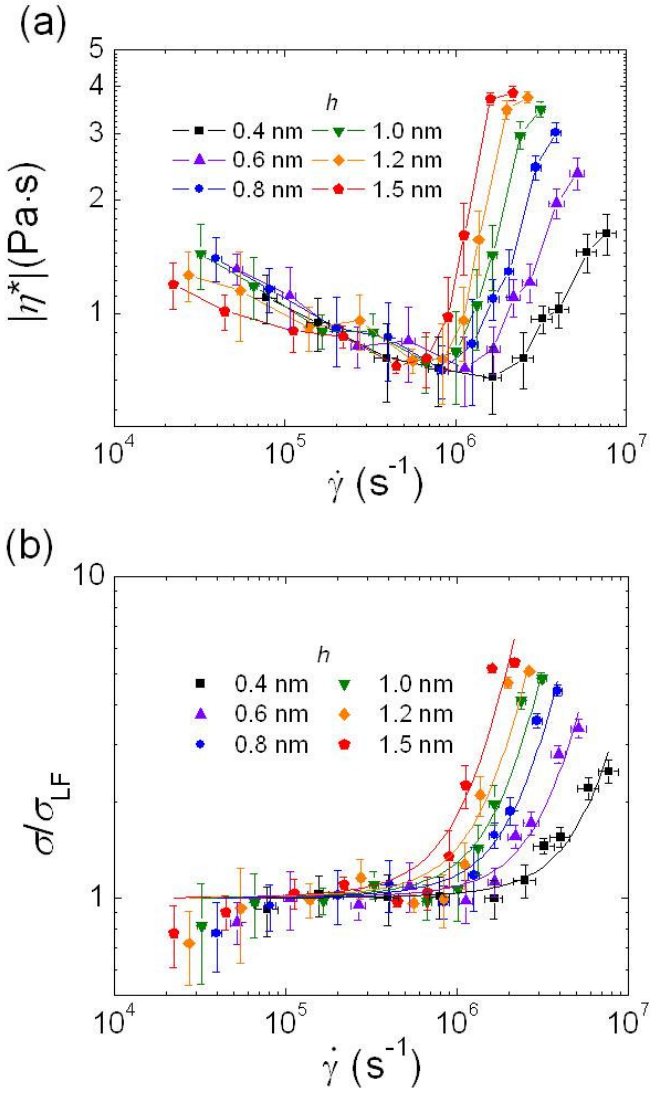

Figure 4.4: (a) Magnitude of complex viscosity $|\eta*| = \sqrt{\eta^2 + (G/\omega)^2}$ represents the total flow resistance included with both viscosity and elasticity. (b) Stress ratio, σ/σ_{LF} , versus shear rate. Stress of HWL is given by $\sigma = |\eta * |\dot{\gamma}$, while stress of LF σ_{LF} is obtained by fitting the region below ET in Fig. 4 (a). huge increase of the ratio confirms enhanced flow resistance due to ET. Each data point represents average of twelve measurements and its error bars correspond to standard deviation.

4.3 Reynolds and Weissenberg number

In hydrodynamics, the Reynolds number (Re) is a dimensionless quantity that used to help predict liquidity characteristics of fluids. Of course, Re is not absolute value to predict liquidity, but let me notice Re is very useful factor in early experimental step [12]. Re is defined as

$$\mathrm{Re} = \frac{\text{inertial forces}}{\text{viscous forces}} = \frac{\rho U L}{\eta} \tag{4.1}$$

where ρ, U, L and η are the density of the fluid, mean velocity of the object relative to the fluid, is a characteristic system size and dynamic viscosity of fluid, respectively. the predicted liquidity characteristics range of fluids occur: (Note: The follow informations are taken from ref. [12]):

$$\begin{aligned}
0 < \mathrm{Re} < 1 \quad &: \text{ laminar flow, creeping motion} \\
1 < \mathrm{Re} < 10^2 \quad &: \text{ laminar, strong Re dependence} \\
10^2 < \mathrm{Re} < 10^3 \quad &: \text{ laminar, boundary layer theory} \\
10^3 < \mathrm{Re} < 10^4 \quad &: \text{ transition to turbulence} \\
10^4 < \mathrm{Re} < 10^6 \quad &: \text{ turbulence, moderate Re dependence} \\
10^4 < \mathrm{Re} < \infty \quad &: \text{ turbulence, slight Re dependence}
\end{aligned} \tag{4.2}$$

On the other hand, Weissenberg number (Wi) is a dimensionless quantity that used to study of viscoelastic flows. Re is defined as

$$\mathrm{Wi} = \text{shear rate} \times \text{relaxation time} = \dot{\gamma}\tau. \tag{4.3}$$

Wi is not well classification as Re, however recent experiments had exhibited that viscoelastic flow transit to elastic turbulence with 1∼30 value of Wi [1, 2, 4, 6].

These two numbers (Re, Wi) are coefficients of nonlinear term of dimnesionless equations described flow. The following equation is the equation of motion of the fluid.

$$\rho \left\{ \frac{\partial \boldsymbol{v}}{\partial t} (\boldsymbol{v} \cdot \bigtriangledown) \right\} = \bigtriangledown \cdot \boldsymbol{\sigma} - \bigtriangledown p \tag{4.4}$$

where $\boldsymbol{v}, \boldsymbol{\sigma}, p$ are the velocity of flow, stress and acted pressure to flow. The stress is given as follow:

$$\boldsymbol{\sigma} + \tau \overset{\bigtriangledown}{\boldsymbol{\sigma}} = \eta_0 \dot{\boldsymbol{\gamma}} \tag{4.5}$$

where $\overset{\bigtriangledown}{\boldsymbol{\sigma}}$ presents convected time derivative of stress tensor studied in chapterer 4.3.3. When relaxation time τ is zero, Eq. (4.4) becomes $Navier-Stokes\ equation$. To change the Eq. (4.4), (4.5) to dimensionless equations, here dimensionless parameters are defined.

$$t' = \frac{tU}{L},\ x_i' = \frac{x_i}{L},\ v_i' = \frac{v_i}{U},\ \sigma_{ij}' = \frac{\sigma L}{\eta U},\ p' = \frac{p}{\rho U^2} \tag{4.6}$$

Inserting Eq.(4.6) into Eq. (4.4) and (4.5), Following dimensionless equations are obtained.

$$\mathrm{Re} \left\{ \frac{\partial \boldsymbol{v'}}{\partial t'} + (\boldsymbol{v'} \cdot \bigtriangledown') \boldsymbol{v'} \right\} = \bigtriangledown' \cdot \boldsymbol{\sigma'} - \mathrm{Re} \bigtriangledown' p' \tag{4.7}$$

$$\boldsymbol{\sigma'} = \dot{\boldsymbol{\gamma}}' - \mathrm{Wi} \overset{\bigtriangledown}{\boldsymbol{\sigma}} \tag{4.8}$$

where Reynolds number and Weissenberg mumber are defined as Re= $\rho UL/\eta$, Wi= $\tau U/L$. If Wi is zero, Eq. (4.7) becomes as follow:

$$\mathrm{Re}\left\{\frac{\partial \boldsymbol{v'}}{\partial t'} + (\boldsymbol{v'}\cdot\bigtriangledown')\boldsymbol{v'}\right\} = \bigtriangledown'\cdot\dot{\boldsymbol{\gamma}}' - \mathrm{Re}\bigtriangledown' p' \tag{4.9}$$

This equation is dimensionless Navier-Stokes equation. Re is put ahead of nonlinear term, $(\boldsymbol{v'}\cdot\bigtriangledown')\boldsymbol{v'}$, called inertia term, and $\bigtriangledown' p'$ which is also could be nonlinear term by form pressure. On the other hand Re is not put ahead of linear term, $\bigtriangledown'\cdot\dot{\boldsymbol{\gamma}}'$, called viscous term. Therefore the more Re increase, the more nonlinearity of flow is large.

Viscoelastic flow has the finite Wi value, thus Eq. (4.7) is given as:

$$\mathrm{Re}\left\{\frac{\partial \boldsymbol{v'}}{\partial t'} + (\boldsymbol{v'}\cdot\bigtriangledown')\boldsymbol{v'}\right\} = \bigtriangledown'\cdot\dot{\boldsymbol{\gamma}}' - \mathrm{Wi}\bigtriangledown'\cdot\overset{\bigtriangledown}{\boldsymbol{\sigma}} - \mathrm{Re}\bigtriangledown' p' \tag{4.10}$$

Wi is put ahead of $\bigtriangledown'\cdot\overset{\bigtriangledown}{\boldsymbol{\sigma}}$ which term is nonlinear. Therefore the Eq. (4.10) remains nonlinear equation when Re go to zero.

4.4 Viscoelastic Model

4.4.1 Liear Maxwell model

The first trying to describe a viscoelastic equation appears to have been that of Maxwell [31], who derveloped a theory for viscoelasticity, since he thought that every gases might be viscoelastic. He propose that viscoelastic fluids could be described by:

$$\boldsymbol{\sigma} + \tau\frac{\partial}{\partial t}\boldsymbol{\sigma} = \eta_0\dot{\boldsymbol{\gamma}}, \tag{4.11}$$

where $\boldsymbol{\sigma}$, $\boldsymbol{\gamma}$, τ and η_0 present stress tensor, strain rate tensor, relaxation time and viscosity, respectively. Note Eq. (4.11) becomes hydrodynamic stress-strain rate relation when the relaxation time, which is the taken time to be stable state after deforming to fluids, becomes zero. The solutions could be easily obtained due to two reasons. (i) every components of tensor equations are independent each other. (ii) the equations are a first-order, linear equations as a function of t as follow:

$$\sigma_{ij}(t) = \mathrm{e}^{-t/\tau} \int_0^t \left\{ \frac{\eta_0}{\tau} \mathrm{e}^{t'/\tau} \right\} \dot{\gamma}_{ij}(t)\, dt. \tag{4.12}$$

If $\dot{\gamma}_{ij}$ is independent t, the solutions are:

$$\sigma_{ij}(t) = \eta \dot{\gamma}_{ij} + \mathrm{C}_0 \mathrm{e}^{-t/\tau}, \tag{4.13}$$

where C_0 is the integral constant. Note that the solutions are the same with hydrodynamic solutions when time is hyge larer than relaxation time ($t \gg \tau$). This model had been successfully described avarious viscoelastic materials with small deformation. However this model could not explain the nonlinearlity of viscoelastic materials results from large deformation. The nonlinear viscoelastic model was proposed by James G. Oldroyd in 1950 [32].

4.4.2 Nonliear Maxwell model

The nonlinear Maxwell model is a general form of linear maxwell model included large deformation. The model is as follow:

$$\boldsymbol{\sigma} + \tau \overset{\nabla}{\boldsymbol{\sigma}} = \eta_0 \dot{\boldsymbol{\gamma}}, \tag{4.14}$$

$$\overset{\triangledown}{\boldsymbol{\sigma}} = \frac{\partial}{\partial t}\boldsymbol{\sigma} + \boldsymbol{v}\cdot\bigtriangledown\boldsymbol{\sigma} - \left\{(\bigtriangledown\boldsymbol{v})^{\dagger}\cdot\boldsymbol{\sigma} + \boldsymbol{\sigma}\cdot\bigtriangledown\boldsymbol{v}\right\} \tag{4.15}$$

where $\overset{\triangledown}{\boldsymbol{\sigma}}$ is the convected time derivative, and $\bigtriangledown\boldsymbol{v}$ is the velocity gradient tensor with ijth component $(\partial/\partial x_i)v_j$. And strain rate tensor could be represent with the velocity gradient tensor:

$$\dot{\boldsymbol{\gamma}} = \bigtriangledown\boldsymbol{v} + (\bigtriangledown\boldsymbol{v})^{\dagger} \tag{4.16}$$

Note that Eq. 4.14 becomes linear Maxwell model when convected time derivative is simply replaced by $\partial\boldsymbol{\sigma}/\partial t$. Components of stress are not independent each other due to mixed term of Eq. (4.15), and these term have the nonlinearity. Before studing of elastic turbulence by shear motion, Let me introduce the simple shear motion in Fig. 4.5. For simple shear flow of homogeneous fluid the stress and shear rate tensor is given as follow:

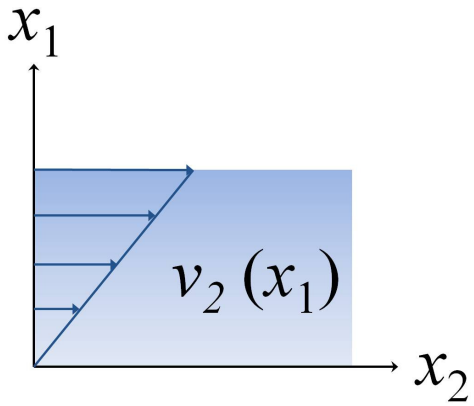

Figure 4.5: Diagram of simple shear motion. The velocity vector of simple shear motion is $(0,\ v_2,\ 0)$ where v_2 is independent of time.

$$\boldsymbol{\sigma} = \begin{pmatrix} \sigma_{11} & \sigma_{12} & 0 \\ \sigma_{12} & \sigma_{22} & 0 \\ 0 & 0 & \sigma_{33} \end{pmatrix}, \quad \bigtriangledown \boldsymbol{v} = \begin{pmatrix} 0 & \dot{\gamma}_{12} & 0 \\ 0 & 0 & 0 \\ 0 & 0 & 0 \end{pmatrix} \tag{4.17}$$

Inserting Eq. (4.17) into Eq. (4.14), then Eq. (4.14) is written as:

$$\left(1 + \tau \frac{\partial}{\partial t}\right) \begin{pmatrix} \sigma_{11} & \sigma_{12} & 0 \\ \sigma_{12} & \sigma_{22} & 0 \\ 0 & 0 & \sigma_{33} \end{pmatrix} - \tau \dot{\gamma}_{12} \begin{pmatrix} 2\sigma_{12} & \sigma_{22} & 0 \\ \sigma_{22} & 0 & 0 \\ 0 & 0 & 0 \end{pmatrix} = \eta \begin{pmatrix} 0 & \dot{\gamma_{12}} & 0 \\ \dot{\gamma_{12}} & 0 & 0 \\ 0 & 0 & 0 \end{pmatrix} \tag{4.18}$$

Note that $\bigtriangledown \boldsymbol{\sigma} = 0$ since the flow is homogeneous so that the stress tensor do not depend on space. Then the solutions are obtained by,

$$\begin{aligned} \sigma_{11} &= 2\eta\tau\dot{\gamma}_{12}^2 + (c_{22}\dot{\gamma}_{12}^2 t^2 + 2c_{12}t + c_{12})\mathrm{e}^{-t/\tau} \\ \sigma_{12} &= \eta\dot{\gamma}_{12} + (c_{22}\dot{\gamma}_{12}t + c_{12})\mathrm{e}^{-t/\tau} \\ \sigma_{22} &= c_{22}\mathrm{e}^{-t/\tau} \\ \sigma_{33} &= c_{33}\mathrm{e}^{-t/\tau} \end{aligned} \tag{4.19}$$

For oscillatory shearing flow, $\dot{\gamma}_{12} = \dot{\gamma}_0 \mathrm{sin}\omega t = (A\omega/h)\mathrm{sin}\omega t$, solutions shear motion are given by,

$$\begin{aligned} \sigma_{12} &= -\eta_0\dot{\gamma}_0 \frac{\tau\omega}{1+\tau^2\omega^2}\mathrm{cos}\omega t + \frac{\eta_0\dot{\gamma}_0}{1+\tau^2\omega^2}\mathrm{sin}\omega t \\ &\quad + \left(\frac{\dot{\gamma}_0}{\omega}\mathrm{c}_{22}\mathrm{cos}\omega t + \mathrm{c}_{12}\right)\mathrm{e}^{-t/\tau} \\ \sigma_{22} &= c_{22}\mathrm{e}^{-t/\tau} \end{aligned} \tag{4.20}$$

The stable total shear stress ($t \gg \tau$) is obtained by magnitude of complex viscosity $\eta*$,

$$\begin{aligned} \sigma_{12} &= \eta_0\dot{\gamma}_0\sqrt{\left(\frac{\tau\omega}{1+\tau^2\omega^2}\right)^2+\left(\frac{1}{1+\tau^2\omega^2}\right)^2} \\ &= \eta_0\dot{\gamma}_0\sqrt{\frac{1}{1+\tau^2\omega^2}} \equiv |\eta*|\dot{\gamma}_0. \end{aligned} \tag{4.21}$$

In the case of nanconfined water and QTF system, the magnitude of complex viscosity is similar to that of η_0 with $\tau \sim 10^{-6}$s and $\omega \sim 2 \times 10^5 \mathrm{s}^{-1}$. ($|\eta*| \approx 0.98 \times \eta_0$).

In this chapter the stress by simple or oscillating shear motion was obtained using linear and nonlinear Maxwell model. However, it is valid to predict increaing stress due to turbulence since these motions present laminar flow. Of course, it will be nice if someone analytically sloves the Eq. (4.4) and (4.5) at given boundary conditions, but it is nearly impossible [21]. Next chapter, I will provide the statistical method where physical properties are decompsed average and fluctuating values.

4.5 Elastic Turbulence in Nonlinear Maxwell Model

4.5.1 Additive Stress via Correlation between Fluctuations

Turbulence includes of random velocity fluctuation, thus the stress and velocity could be decomposed into their respective mean and fluctuation value as follows [20]:

$$\boldsymbol{\sigma} = \bar{\boldsymbol{\sigma}} + \boldsymbol{\sigma'} = \begin{pmatrix} \bar{\sigma}_{11} + s_{11} & \bar{\sigma}_{12} + s_{12} & s_{13} \\ \bar{\sigma}_{12} + s_{12} & \bar{\sigma}_{22} + s_{22} & s_{23} \\ s_{13} & s_{23} & \bar{\sigma}_{33} + s_{33} \end{pmatrix}, \tag{4.22}$$

$$\begin{aligned} \bigtriangledown \boldsymbol{v} &= \bigtriangledown(\bar{\boldsymbol{v}} + \boldsymbol{v'}) = \begin{pmatrix} \partial_x \\ \partial_y \\ \partial_z \end{pmatrix} \begin{pmatrix} \bar{v}_x(y) + v'_x & v'_y & v'_z \end{pmatrix} \\ &= \begin{pmatrix} \dot{\epsilon}_{11} & \dot{\epsilon}_{12} & \dot{\epsilon}_{13} \\ \bar{\dot{\gamma}}_{12} + \dot{\epsilon}_{12} & \dot{\epsilon}_{22} & \dot{\epsilon}_{23} \\ \dot{\epsilon}_{13} & \dot{\epsilon}_{23} & \dot{\epsilon}_{33} \end{pmatrix}, \end{aligned} \tag{4.23}$$

where $\partial_x = \partial/\partial x$, $\dot{\epsilon_{ij}} = (\partial/\partial x_i)v'_j$ is the fluctuation of strain rate, v'_i is the fluctuation of velocity, s_{ij} the fluctuation of stess, and over-bar denotes average values. Inserting equation 4.22, 4.23 into equation 4.14, the equation of shear

component is obtained by,

$$(1+\partial_t)(\bar{\sigma}_{12}+s_{12})-\tau\left[(\bigtriangledown \boldsymbol{v})^{\dagger}\cdot\boldsymbol{\sigma}+\boldsymbol{\sigma}\cdot\bigtriangledown\boldsymbol{v}\right]_{12}=\eta(\bar{\dot{\gamma}}_{12}+\dot{\epsilon}_{12}), \tag{4.24}$$

$$\begin{aligned}\left[(\bigtriangledown \boldsymbol{v})^{\dagger}\cdot\boldsymbol{\sigma}+\boldsymbol{\sigma}\cdot\bigtriangledown\boldsymbol{v}\right]_{12} &= \dot{\epsilon}_{11}(\bar{\sigma}_{12}+s_{12})+\dot{\epsilon}_{12}(\bar{\sigma}_{11}+s_{11}) \\ &+\dot{\epsilon}_{22}(\bar{\sigma}_{12}+s_{12})+(\bar{\dot{\sigma}}_{12}+\dot{\epsilon}_{12})(\bar{\sigma}_{22}+s_{22})+\dot{\epsilon}_{32}s_{13}+\dot{\epsilon}_{13}s_{32}.\end{aligned} \tag{4.25}$$

By taking emsemble average of all terms in Eq. (4.25), we obtain

$$\bar{\sigma}_{12}+\tau\partial_t\bar{\sigma}_{12}-\tau\bar{\dot{\gamma}}_{12}\bar{\sigma}_{22}-\tau\sum_{i=1}^{3}\left(\langle s_{1i}\dot{\epsilon}_{i2}\rangle+\langle\dot{\epsilon}_{1i}s_{i2}\rangle\right)=\eta\bar{\dot{\gamma}}_{12} \tag{4.26}$$

where $\langle\bar{A}\rangle=\bar{A}$, $\langle a'\rangle=0$, $\langle\bar{A}a'\rangle=\bar{A}\langle a'\rangle=0$, and $\langle\partial_t A\rangle=\partial_t\langle A\rangle$ ($\bar{A}$ is the average value of a quantity and A the a' fluctuation). Note that the net effect of fluctuation in Eq. (4.26) is the additional stress term associated with elastic turbulence, denoted by σ_{ET},

$$\sigma_{\mathrm{ET}}=\tau\sum_{i=1}^{3}\left(\langle s_{1i}\dot{\epsilon}_{i2}\rangle+\langle\dot{\epsilon}_{1i}s_{i2}\rangle\right), \tag{4.27}$$

which indicates that the correlation between fluctuations of stress and strain rate enhances the shear stress.

4.5.2 Scaling of Additive Stress

The additive stress tensor is composed by the correlation between fluctuations of stress and strain rate. If we know the relation between fluctuations of stress and strain rate, Eq. 4.27 could be changed the correlation between fluctuations

of strain rate. The fluctuations are still satisfied the nonlinear Maxwell model, then the relation between fluctuations of stress and strain rate as follow,

$$s_{ij} \approx \eta_0 \dot{\epsilon}_{ij} + \tau \sum_{k=1}^{3} \left(\langle s_{ik} \dot{\epsilon}_{kj} \rangle + \langle \dot{\epsilon}_{ik} s_{kj} \rangle \right), \tag{4.28}$$

where the first term of right hand side is linear term. This term is still remained when the fluctuations are small, and are satisfied the linear model. On the other hand, if the fluctuation is large mix term, we again consider the additive stress term where the fluctuations are mixed with other components of strain rate and stress which is originated by convected derivative of nonlinear Maxwell model. Putting again Eq. 4.28 in other components of the stress fluctuations in Eq. 4.28, we could obtain the equation as follow,

$$\begin{aligned} s_{ij} \approx \eta_0 \dot{\epsilon}_{ij} + \tau \sum_{k=1}^{3} \Bigg[\dot{\epsilon}_{ik} \left(\eta_0 \dot{\epsilon}_{kj} + \tau \sum_{l=1}^{3} \left(\langle s_{kl} \dot{\epsilon}_{lj} \rangle + \langle \dot{\epsilon}_{kl} s_{lj} \rangle \right) \right) \\ + \left(\eta_0 \dot{\epsilon}_{ik} + \tau \sum_{l=1}^{3} \left(\langle s_{il} \dot{\epsilon}_{lk} \rangle + \langle \dot{\epsilon}_{il} s_{lk} \rangle \right) \right) \Bigg], \end{aligned} \tag{4.29}$$

As a result, the relation between fluctuations of the stress and strain rate becomes as

$$s_{ij} \approx \eta_0 \dot{\epsilon}_{ij} + \tau \sum_{k=1}^{3} \left(2\eta_0 \dot{\epsilon}_{ik} \dot{\epsilon}_{kj} + 4 \sum_{l=1}^{3} \eta_0 \dot{\epsilon}_{ik} \dot{\epsilon}_{kl} \dot{\epsilon}_{lj}, \right), \tag{4.30}$$

Inserting Eq. 4.30 into Eq. 4.27, the additive stress term could be obtained the following form.

$$\begin{aligned} \sigma_{\mathrm{ET}} \approx \tau \sum_{i=1}^{3} \Bigg\langle \dot{\epsilon}_{1i} \left[\eta_0 \dot{\epsilon}_{i2} + \tau \sum_{k=1}^{3} \left(2\eta_0 \dot{\epsilon}_{ik} \dot{\epsilon}_{k2} + 4\tau \sum_{l=1}^{3} \eta_0 \dot{\epsilon}_{1k} \dot{\epsilon}_{kl} \dot{\epsilon}_{l2} \right) \right] \Bigg\rangle \\ + \left\langle \left[\eta_0 \dot{\epsilon}_{1i} + \tau \sum_{k=1}^{3} \left(2\eta_0 \dot{\epsilon}_{1k} \dot{\epsilon}_{ki} + 4\tau \sum_{l=1}^{3} \eta_0 \dot{\epsilon}_{1k} \dot{\epsilon}_{kl} \dot{\epsilon}_{li} \right) \right] \dot{\epsilon}_{i2} \right\rangle. \end{aligned} \tag{4.31}$$

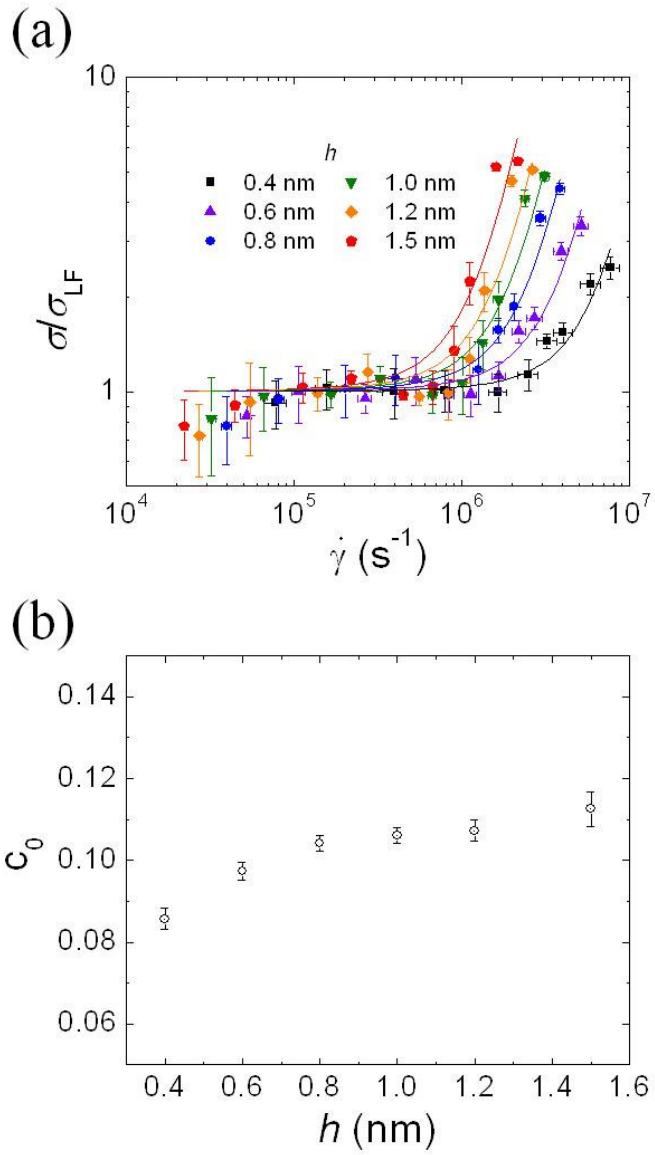

Figure 4.6: Fitting of the stress ratio. (a) Eq. (4.33) versus $\dot{\gamma}_0$ for various distance h, showing good agreement with experimental results. (b) Fitting parameter c_0 shows an overall value of 0.1, indicating that the fluctuation is 10 times smaller than the average shear rate. Slight increase of c_0 with h suggests similar increase of fluctuation is accompanied, producing ET a little easier, as also observed in the decrease of with h.

Let us try to find simple scaling behaviour of the additive stress tensor. If we assume the magnitude of fluctuations of the strain rate is similar each other components, and fluctuations increases with the amplitude of shear rate, one can expand $\dot{\epsilon}_{ij}$ in power series, $\dot{\epsilon}_{ij} \approx c_0\bar{\dot{\gamma}}_0 + O(\dot{\gamma}_0^2)$ where c_0 is constant meant relative magnitude of fluctuation compared with average shear rate. Then we could present additive stress term as Weissenberg number($Wi = \tau\dot{\gamma}_0$).

$$\sigma_{ET} \approx 6\eta_0\tau {c_0}^2\dot{\gamma}_0^2 + 6^2\eta_0\tau^2 {c_0}^3\dot{\gamma}_0^3 + 6^3\eta_0\tau^3 {c_0}^4\dot{\gamma}_0^4 \tag{4.32}$$

Inserting Eq. 4.33 into Eq. 4.26 and 4.27, we calculate the stress ratio,

$$\sigma_{12}/\sigma_{LF} \approx 1 + (6\tau {c_0}^2\dot{\gamma}_0 + 6^2\tau^2 {c_0}^3\dot{\gamma}_0^2 + 6^3\tau^3 {c_0}^4\dot{\gamma}_0^3) \tag{4.33}$$

Figure 4.6 presents the time-averaged experimental data, which is well fitted by the ensemble-averaged stress ratio (Eq.4.33). Here, τ is obtained as the inverse of the threshold shear rate (Fig. 4.7 (a)). Notice that there is only one fitting parameter c_0 for plotting equation (Eq.4.33), which shows an overall value of 0.1, indicating that the fluctuation is 10 times smaller than the average shear rate.

4.6 Fluidity of Confined HWL

As various viscoelastic fluids have shown experimental evidence of ET for 1<Wi<30 [1, 4, 6, 17], we confirm similar behaviours in Fig. 4.7 (a): the threshold value $Wi_{th} = \dot{\gamma}_{th}\tau_M$ lies between 1 and 30 ($\tau_M = k/(b\omega^2)$ is the dynamic relaxation

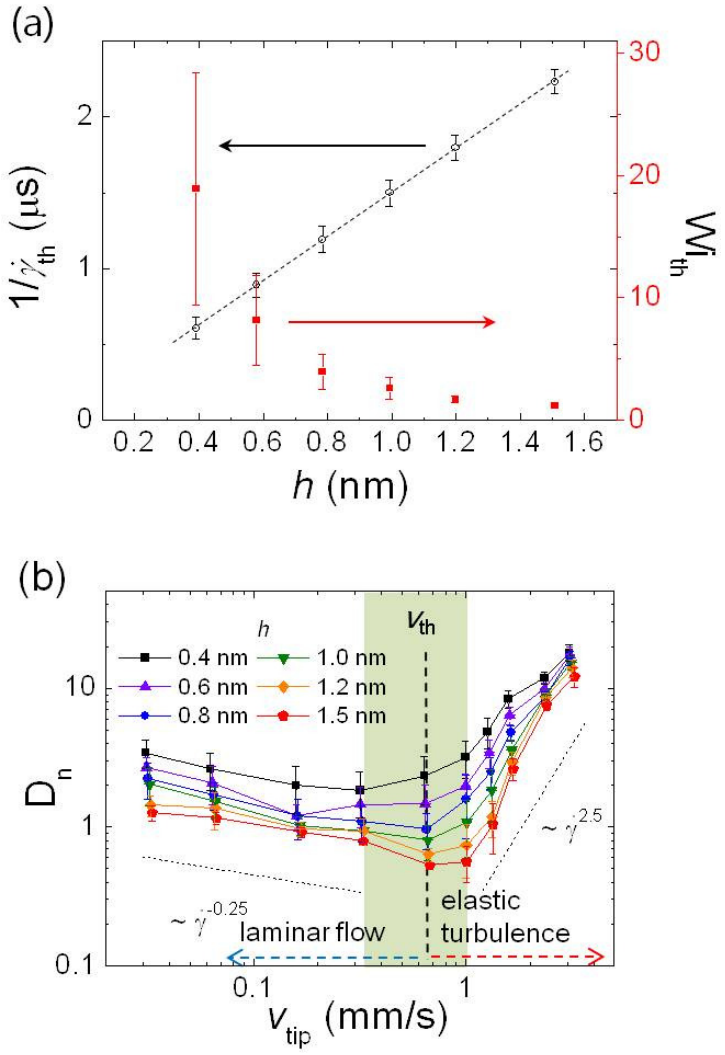

Figure 4.7: Behaviors of threshold region and autoregulation of capillary flow. (a) The inverse threshold values of shear rate $1/\dot{\gamma}_{\mathrm{th}}$ and Weissenberg numbers $\mathrm{Wi}_{\mathrm{th}}$ versus h are in good agreement with observations in polymer solution. The dotted line is proportional to h, which indicates ET occurs at a constant velocity, independent of h, because $1/\dot{\gamma}_{\mathrm{th}} \approx h/v_{\mathrm{th}}$. (b) Variation of the Deborah number $\mathrm{D_n}$ versus $\mathrm{v_{tip}}$ by the power law, $\mathrm{D}_n \propto v_{\mathrm{tip}}^{\beta}$. The threshold velocity is measured as 0.7±0.3 mm/s (green color region). As observed, β is ($\sim$ -0.25) below $\mathrm{v_{th}}$ and $\sim$2.5 above $\mathrm{v_{th}}$, which indicates the high shear rate augments the solidity of HWL when $\mathrm{v_{tip}}$ exceeds $\mathrm{v_{th}}$, whereas the solidity decreases as $\mathrm{v_{tip}}$ increases below vth. Each data point represents average of twelve measurements and its error bars correspond to standard deviation.

time in the Maxwell model [21]) and becomes smaller at larger h, as also observed in polymer solution [1]. Notice that the linear increase of $1/\dot{\gamma}_{\rm th}$ versus h (Fig. 4.7 (a)) indicates the threshold velocity $v_{\rm th}$ is independent of h since $\dot{\gamma}_{\rm th} \approx v_{\rm th}/h$, which suggests it is illuminating to address ET versus the shear-flow velocity rather than the shear rate.

Figure 4.7 (b) plots the Deborah number $\mathrm{D_n}(= \tau_{\rm M}\omega)$, the measure of solidity of viscoelastic flow [22], versus $v_{\rm tip}$. As shown, Fig. 4.7 (b) exhibits dynamic transition to nonlinear fluidity at the fixed $v_{\rm th} = 0.7 \pm 0.3$ mm/s. Moreover, the power law $\mathrm{D_n} \propto v_{\rm tip}^{\beta}$ implies that when $\beta < 1$, $\mathrm{D_n}$ decreases with $v_{\rm tip}$ (i.e., liquidlike flow) whereas when $\beta > 1$, the flow becomes stiff with $v_{\rm tip}$, being more solidlike. Interestingly, Fig. 4.7 (b) shows β changes discretely from -0.25 to 2.5 at $v_{\rm th}$, independent of h, demonstrating the liquidity-to-solidity transition in HWL or the occurrence of ET. Notice that the transition becomes less pronounced as h decreases.

4.7 Understanding of Autoregulation in capillary via ET

Figure 4.8 (a) presents the more explicit characteristics of ET in the behaviour of $|\eta|*$; sharp increase of $|\eta|*$ near $v_{\rm th}$, independent of h, unlike the h-dependent $\dot{\gamma}_{\rm th}$ (Fig. 4.8 (a)). In polymer experiments, the enhanced stress or flowresistance was attributed to the stretched polymer molecules in solution due to ET [1]. Computer simulations on confined water between two hydrophilic surfaces show that

the surfaces are interrelated by the hydrogen-bond network when they are close enough [15] and the correlation time between hydrogen bonds becomes longer than in bulk water [16], as discussed in the sluggish dynamics of Nanoconfiend water in Fig. 4.8 (a). Therefore, the enhancement of flow resistance in nanoconfiend HWL associated with ET, resulting from the fluctuation-induced correlation, could be also attributed to the similarly 'stretched' or hydrogen-bond network that consists of water molecules and hydration layers.

Interestingly, in Fig. 4.8 (a), we observe $|\eta|*$ decreases slightly with v_{tip} whereas it sharply increases above threshold, which results in a stable equilibrium velocity at 0.7±0.3 mm/s. This fluid dynamic peculiarity of NW may be critical to physical understanding of mechanics in various nano-confined liquids including water. For example, it may account for autoregulation of capillary blood flow and our results are in striking agreement with the measured average velocity ($\sim$ 1 mm/s) of red blood cells (RBCs) in capillaries [10]. Because RBCs are on average 25% larger than capillaries [23], they become severely deformed and literally plugging [24] so that nanometric plasma (90% water) layer forms between RBCs and less-deformable capillary [25], as schematized in Fig. 4.8 (d). Except some possible pathological origins for autoregulation [26, 27], fluid dynamics of plasma layer still remains unaddressed despite its crucial role in blood rheology [25, 28] and autoregulation. However, our results suggest that RBCs experience enhanced flow resistance by ET in plasma layer when RBC flow velocity exceeds $\sim$ 1mm/s. Moreover, Fig. 4.8 (a) explains the steady and stable blood flow in capillaries despite normal blood-pressure variation. Moreover,

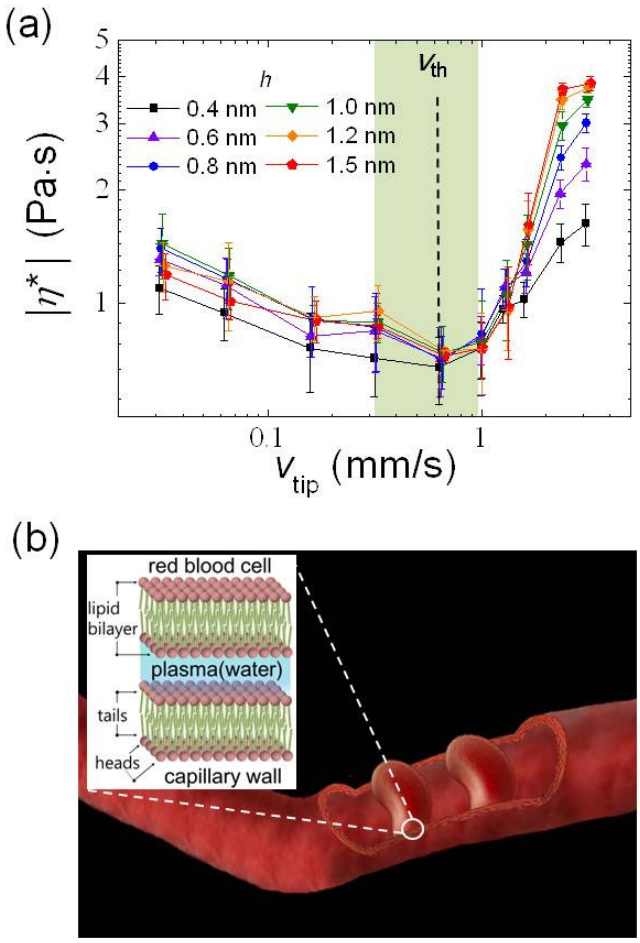

Figure 4.8: (a) Apparent viscosity (or magnitude of complex viscosity) versus v_{tip}. Whereas $|\eta*|$ decreases with v_{tip} below v_{th}, it hugely increases above v_{th}, independent of h, which suggests a universal characteristic associated with hydrodynamics of HWL. Each data point represents average of twelve measurements and its error bars correspond to standard deviation. (b) Erythrocytes flow in capillaries steadily at $\sim$1 mm/s despite normal blood-pressure change. Because RBCs are easily deformed in capillaries which diameter are on average smaller than RBCs, ultrathin plasma layer is formed between the Erythrocyte-capillary gap, whose hydrodynamic properties can be investigated from those of HWL. Inset shows plasma layer formed between two lipid-bilayer cell membranes of relatively flexible Erythrocytes and more-stiffer capillary wall. The cells are generally covered by hydration layer because of the hydrophilic characteristic of lipid-bilayer head group [30].

slight decrease of $|\eta|*$ with vtip below threshold (Fig. 4.8 (a)) is also consistent with the observed viscosity decrease of RBCs in microvessels versus the RBC velocity under $\sim$ 1 mm/s [29].

4.8 Conclusion

In conclusion, The existence of elastic turbulence between hydrophilic surfaces is shown where Reynolds number is nearly zero. In nanoconfined water, the flow resistance increases when the flow velocity is lareger than $\sim 0.7 \pm 0.3$ mm/s (or above the threshold shear rate, $\dot{\gamma}_{\mathrm{th}} \sim 10^6$ s^{-1}). Theoretical analysis indicates ET is occurred with correlation between fluctuations of shear rate and stress. This results suggest physical understanding of autoregulation, which is the phenomenon of maintain slow ($\sim$1 mm/s) and steady flow in spite of blood-pressure change, in brain capillaries, as due to ET in nanoconfined water between red blood cell and capillary wall.

Bibliography

[1] A. Groisman and V. Steinberg, Nature **405**, 53 (2000).

[2] A. Groisman and V. Steinberg, Nature **410**, 905 (2001).

[3] S. Lerouge, M. Argentina, and J. Decruppe, Phys. Rev. Lett. **96**, 088301 (2006).

[4] M. Fardin, D. Lopez, J. Croso, G. Gregoire, O. Cardoso, G. McKinley, and S. Lerouge, Phys. Rev. Lett. **104**, 178303 (2010).

[5] D. Samanta, Y. Dubief, M. Holzner, C. Schafer, A. Morozov, C. Wagner, and B. Hof, Proc. Natl. Acad. Sci. **110**, 10557 (2013).

[6] L. Pan, A. Morozov, C. Wagner, and P. Arratia, Phys. Rev. Lett. **110**, 174502 (2013).

[7] R. Larson, Nature **405**, 27 (2000).

[8] T. Li, and E. Riedo, Phys. Rev. Lett. **100**, 106102 (2008).

[9] B. MacVicar and M. Salter Nature **443**, 642 (2006).

[10] A. Hudetz, G. Feher, C. Weigle, D. Knuese, and J. Kampine, Am. J. Physiol. **268**, H2202 (1995).

[11] Y. Itoh and N. Suzuki, J. Cereb. Blood Flow Metab. **32**, 1167 (2012).

[12] F. White *Fluid Mechanics* (Mc Graw Hill Press, 2004).

[13] G. Whitesides Nature **442**, 368 (2006).

[14] M. Lee, B. Sung, N. Hashemi, and W. Jhe, Faraday Discuss. **141**, 415 (2009).

[15] R. Major, E. Houston, M. McGrath, J. Siepmann, and X. Zhu, Phys. Rev. Lett. **96**, 177803 (2006).

[16] Y. Leng, and P. Cummings, Phys. Rev. Lett. **94**, 026101 (2005).

[17] S. Berti, A. Bistagnino, G. Boffetta, A. Celani, and S Musacchio, Phys. Rev. E **77**, 055306 (2008).

[18] R. Bird, R. Armstrong, and O. Hassager *Dynamics of polymeric liquids: Volume 1 Fluid mechanics* (Wiley-Interscience press, 1987).

[19] O. Reynolds, Phil. Trans. R. Soc. Lond. A. **186**, 123 (1895).

[20] H. Tennekes, and J. Lumley *A first course in turbulence* (The MIT Press, 1972).

[21] S. Jeffery, P. Hoffmann, J. Pethica, C. Ramanujan, O. Ozer, and A. Oral, Phys. Rev. B **70**, 054114 (2004).

[22] R. Larson, *The structure and rheology of complex fluids* (Oxford University press, 1999).

[23] G. Snyder and B. Sheafor, Amer. Zool. **39**, 189 (1999).

[24] R. Skalak and P. Branemark, Science **164**, 717 (1969).

[25] R. Whitmore, Nature**215**, 123 (1967).

[26] C. Peppiatt, C. Howarth, P. Mobbs, and D. Attwell, Nature **443**, 700 (2006).

[27] F. Fernandez-Klett, N. Offenhauser, U. Dirnagl, J. Priller, and U. Lindauer, Proc. Atl. Acad. Sci. **51**, 22290 (2010).

[28] G. Mchedlishvili, M. Varazashvili, A. Mamaladze, and N. Momtselidze)Microvas. Res. **53**, 201 (1997).

[29] M. Sugihara-Seki and B. Fu, Fluid Dyn. Res. **37**, 82 (2015).

[30] D. Krepkiy, M. Mihailescu, J. Freites, E. Schow, D. Worcester, K. Gawrisch, D. Tobias, S. White, and K. Swartz, Nature **462**, 473 (2009).

[31] J. C. Maxwell, Phil. Trans. Roy. Soc., **A157**, 49 (1867).

[32] J. G. Oldroyd, Proceedings of the Royal Society of London. Series A, **200**, 523 (1950).

Chapter 5

Conclusions

Nanoconfiend water exists ubiquitously in our environment, and it plays an important role in various mechanism of nature. Nevertheless, it is yet the lack of a sense of an existance of the nanoconfined water, and the studies about it are also not sufficient. The nanoconfined water has obviously different properties compared with bulk water, the properties change evidently depend on how hydrophilic the enclosed surfces are. Among them, this thesis study about fluid dynamic properties of nanoconfined thin water film between hydrophilic surfaces where hydrophiilc surfaces form thin water molecular layers called hydration layer due to stong binding force between water molecules and charged surfaces. Over the last decade, confined hydration water layer has studied using vairous experiment equipments and computer simulation, however the understanding of its dynamics is yet stayed phenomenological results.

Unified hydration stress tensor shows that measured various mechani-

cal properties of confiend hydration water layer, such as normal force, tapping viscoelasticity and shear viscoelasticity, are based on hydration force. And relations between properties are clearly assured via the Unified hydration stress tensor. Moreover new physical properties, Poisson's raito and volume viscosity, are obtained via the relations between shear and tapping measurment using atomic force microscopy.

Other significant phenomenon in confined hydration water layer is the nanoscale elastic turbulence. In Newtonian flow, the turbulence needs an impossible velocity ($\sim 10^6$ m/s) in nanoscale. However the confined hydration water layer could occur the turbulence by viscoelastic property rather than inertia of flow. And, theoretically, it is shown the turbulence is raised via correlation between fluctuations of strain rate and stress. Futhermore the elastic turbulence suggest physical understanding of autoregulation, in brain capillaries. The complete understanding of autoregulation in capillaries would be fulfilled by pathological analyses and additional physical analysis.

The study about nanoconfined water is still in its early stages. Although natural surfaces are formed roughly and heterogeneously, most experiments including this study had performed at atomically flat and homogeneous surfaces. And although the significance of caprillary bridge has emphasized in the past few decades, it has been seldom investigated since it is extremely difficult to deal stable nano water bridge. And it is uncertain whether the theories about water bridge, such as Kelvin equation and Young-Laplace equation, are still adaptable in nanoscale. The hydration force has failed to computer modeling

as well as theoretical work. Above these, the physical role of additive ions, transmissive mechanism of water in nano-pore, and electric field effect etc., unrevealed subjects are remained. Nevertheless the studies in the thesis extend the understanding of the nanoconfiend water between hydrophilic surfaces, although it is the specific study of characterestics in nanoconfiend water, since numerous materials, especially bio molecules, are covered hydrophilic surfaces and the nanoconfined space is certainly filled with liquid water in nature. These studies would contribute to the tribolgy between various surfaces and Rheology of various viscoelastic materials.

초 록

물속뿐만 아니라, 공기 중에서도 대부분의 나노미터 크기의 공간에는 액체 물로 채워져 있다. 따라서 나노컨파인드 물은 우리 주변 어디에나 흔하게 존재하며, 자연히 세포간 상호작용, 점토질의 부품현상, 마찰 등의 다양한 자연계의 메커니즘에 중요한 역할을 한다. 하지만 나노컨파인드 물의 본격적인 연구는 공기중이나 물 안의 나노사이즈의 공간이 컨트롤이 가능해진 21세기가 되면서 활발히 진행되었다. 지난 10여 년간, 밝혀진 나노컨파인드 물의 특성은 다음과 같다. (i) 벌크 물에 비해 $10^2 \sim 10^7$ 배 큰 점성, (ii) 긴 완화시간 ($10^{-2} \sim 10^{-9}$ s), (iii) 비선형 점탄성, (iv) 기존의 면사이 힘 (interfacial force)의 불가. 이렇게 다양한 나노컨파인드 물의 특성이 현상학적으로 밝혀졌지만 (1) 근본적인 특성이나, 특성간 관계에 대한 이해는 여전히 불충분하다. (2) 또한 지금까지는 자연계에서 일어나는 마찰의 속력보다 매우 느린 1 μm/s 이하에서 실험이 시행되었다.

본 연구에서는, (1) 나노컨파인드 수화층의 통합된 응력 텐서 (Unified stress tensor) 가 소개되었으며, 수정진동자를 이용한 원자힘 현미경을 통해 이에 대한 타당성을 검증하였다. 통합된 응력 텐서는 친수성 표면 사이의 나노컨파인드 물의 특성 간 관계를 설명해줄 뿐 아니라 그 관계를 통해서 새로운 물리량을 예측하였다. 그리고 (2) 빠른 속력의 실험 ($\sim$ 1 mm/s)을 통해 뉴턴유체에서는 결코 발생할 수 없는 경이로운 나노스케일의 탄성난류를 관측하였다. 이런 탄성난류는 아직 분명히 이해되지 못한 모세혈관의 자기조절 (Autoregulation) 현상에 물리적 이해를 주었다.

통합된 응력 텐서에 대한 연구는 나노컨파인드 물의 이해를 넓힐 뿐 아니라, 다양한 점탄성 물체의 연구에도 방법론적으로 응용이 될 것이다. 탄성난류에 대한 연구는 나노컨파인드 물이 중요한 역할을 하는 곳에서의 마찰 연구에는 대부분 고려되어 질 것으로 기대한다. 특히 모세혈관의 자기조절 현상의 물리적 이해는 모세혈관의 혈류가 중요하게 고려되는 뇌경색이나 치매 연구에 도움을 줄 것이다.

주요어 : 나노컨파인드물, 수화층, 점탄성, 탄성난류, 원자힘현미경,

학 번 : 2007-20410